Journal of Medicinal Chemistry

pubs.acs.org/jmc

Article

Discovery of LC-MI-3: A Potent and Orally Bioavailable Degrader of Interleukin-1 Receptor-Associated Kinase 4 for the Treatment of Inflammatory Diseases

Lingfeng Chen,*[,#] Ruixiang Luo,[#] Lin Ma,[#] Ying Xu,[#] Jiaqi Cao, Zheng Jiang, Shiyan Chen, Xiaohao Huang, Mingwan Zhang, Lei Zheng, Yawen Zhang, Lina Yin, Jie Yu, Xiaochun Zheng, Lulu Zheng, Ping Huang, and Guang Liang*

Cite This: *J. Med. Chem.* 2024, 67, 8060−8076

Read Online

ACCESS | Metrics & More | Article Recommendations | Supporting Information

ABSTRACT: Interleukin-1 receptor-associated kinase 4 (IRAK4) is a promising therapeutic target in inflammation-related diseases. However, the inhibition of IRAK4 kinase activity may lead to moderate anti-inflammatory efficacy owing to the dual role of IRAK4 as an active kinase and a scaffolding protein. Herein, we report the design, synthesis, and biological evaluation of an efficient and selective IRAK4 proteolysis-targeting chimeric molecule that eliminates IRAK4 scaffolding functions. The most potent compound, LC-MI-3, effectively degraded cellular IRAK4, with a half-maximal degradation concentration of 47.3 nM. LC-MI-3 effectively inhibited the activation of downstream nuclear factor-κB signaling and exerted more potent pharmacological effects than traditional kinase inhibitors. Furthermore, LC-MI-3 exerted significant therapeutic effects in lipopolysaccharide- and *Escherichia coli*-induced acute and chronic inflammatory skin models compared with kinase inhibitors *in vivo*. Therefore, LC-MI-3 is a candidate IRAK4 degrader in alternative targeting strategies and advanced drug development.

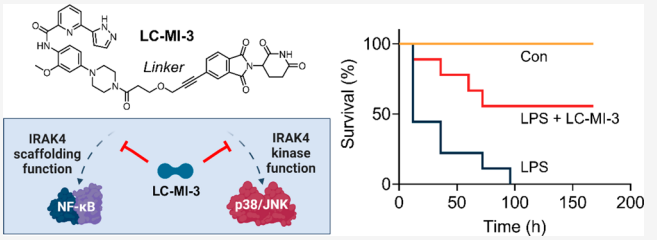

1. INTRODUCTION

Toll-like receptors (TLRs) play a central role in host defense and inflammation by recognizing damage-associated and pathogen-associated molecular patterns.[1] Interleukin-1 receptor (IL-1R)-activated kinase 4 (IRAK4) is a serine/threonine kinase located at the intersection of TLR and IL-1R signaling.[2] It plays important roles in the TLR/IL-1R-mediated myeloid differentiation primary response 88 (MyD88)-dependent signaling pathways.[3] Besides oncological diseases, dysregulation of IRAK4 also implicates inflammatory conditions, such as sepsis, psoriasis, systemic lupus erythematosus, and rheumatoid arthritis.[4] IRAK4 serves as a therapeutic target in chronic inflammatory skin diseases.[5] Therefore, targeting IRAK4 is an attractive therapeutic strategy for autoimmune and inflammatory disorders.[3]

IRAK4 comprises N-terminal death and kinase domains (Figure 1A).[3] Upon TLR ligand binding, IRAKs and MyD88 form a signalosome, termed as "myddosome," a complex consisting of proteins carrying the death domain (IRAKs and MyD88).[1,6] Formation of the myddosome brings the IRAK4 kinase domains into close proximity, enabling IRAK4 trans-phosphorylation (Figure 1B).[7] Phosphorylated IRAK4 further induces IRAK1 phosphorylation and mediates downstream inflammatory signaling via multiple cascades. Several IRAK4 inhibitors, including PF-06650833,[8] BAY-1830839,[9] zabedosertib,[10] edecesertib,[11] and emavusertib,[12] are currently undergoing clinical trials (Figure 1C).

Interestingly, recent studies have reported the dual roles of IRAK4 in the myddosome complex (Figure 1A-B). Although the kinase activity is essential for the recruitment of IRAK1, it is not necessary for the recruitment of IRAK4 to MyD88.[13] Inhibition of IRAK4 kinase activity by a small-molecule compound results in a significantly more stabilized myddosome complex.[14] In addition, IRAK4 kinase activity is not essential for TLR4 signaling; however, IRAK4 scaffold function is essential for nuclear factor (NF)-κB activation in TLR4-activated macrophages.[15] The IRAK4 death domain is essential for receptor proximal signaling by mediating TLR-induced NF-κB activation.[16] IRAK4 also exhibits a critical scaffold function in myddosome formation, but its kinase activity is not essential for myddosome assembly. Although a modest therapeutic effect was observed in rheumatoid arthritis in a clinical trial using PF-06650833, this IRAK4 kinase inhibitor did not show

Received: January 21, 2024
Revised: April 24, 2024
Accepted: April 26, 2024
Published: May 9, 2024

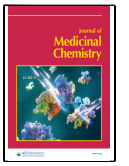

https://doi.org/10.1021/acs.jmedchem.4c00181
J. Med. Chem. 2024, 67, 8060−8076

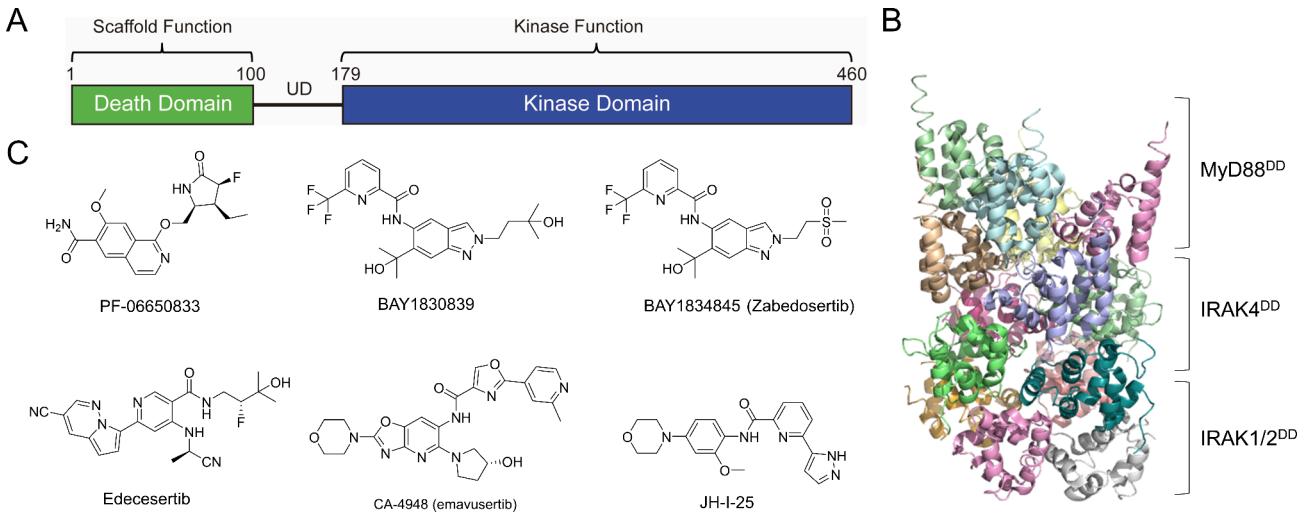

Figure 1. Interleukin-1 receptor-associated kinase 4 (IRAK4) and recently developed IRAK inhibitors. (A) Schematic representation of IRAK4 domains. UD, undetermined domain. (B) Death domain (DD) of MyD88, IRAK4, and IRAK2 form the myddosome complex (PDB ID: 3MOP). (C) Chemical structures of the recently developed IRAK4 inhibitors.

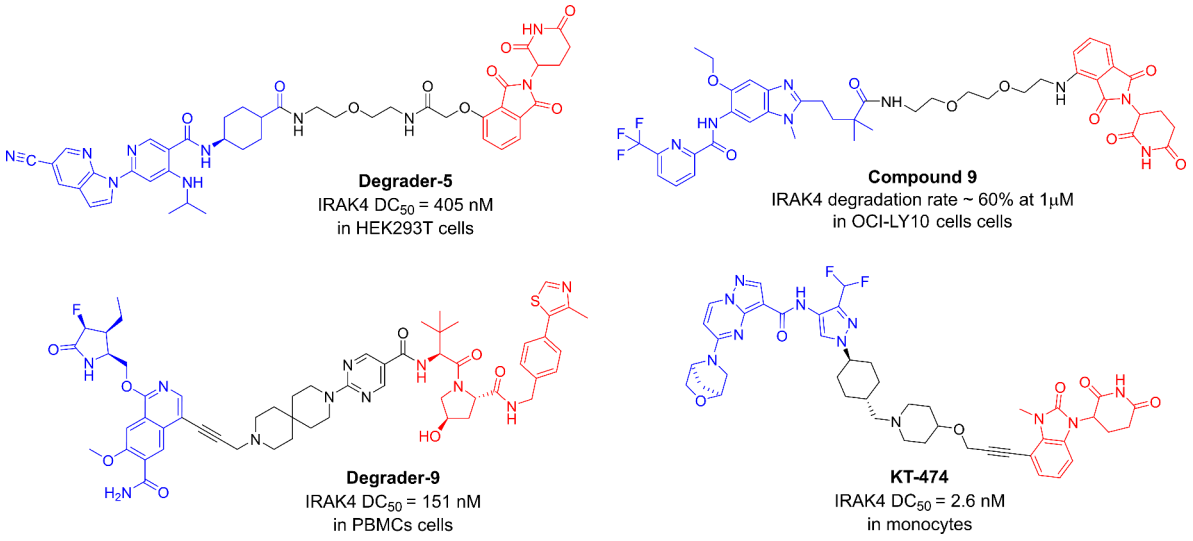

Figure 2. Chemical structures of reported IRAK4 degraders along with their degradation activities.

significant activity in a phase II trial of hidradenitis suppurativa compared to placebo.[17] Therefore, inhibition of the scaffolding function of IRAK4 may cause increased efficacy in the treatment of inflammatory and autoimmune diseases.

The recently developed proteolysis-targeting chimera (PROTAC) technology can simultaneously regulate the catalytic and nonenzymatic functions of target proteins, thereby providing a potential strategy to overcome the limitations of IRAK4 inhibitors (Figure 2).[18] PROTAC are heterobifunctional molecules that induce ubiquitylation of the protein of interest (POI) and promote its degradation via the ubiquitin−proteasome system.[19] Currently, only a few PROTAC have been designed to interfere with the non-enzymatic functions of kinases, such as AURORA-A[20] and focal adhesion kinase,[21] and nonkinase targets.[22,23] Eliminating the IRAK4 scaffold from the myddosome by PROTAC may inhibit all downstream signaling of TLR, thereby blocking inflammation activation and cytokine production.

IRAK4 degraders are an important direction for drug development. Recently developed IRAK1/4 degraders, including degrader-5[24] and compound 9,[25] have shown efficacy in the treatment of activated B-cell-like diffuse large B-cell lymphoma with *MyD88* mutations (Figure 1B). Various IRAK4 degraders, such as degrader 9[26] and KT-474,[17] have been designed for the treatment of inflammation-related diseases. KT-474 has entered phase II clinical trials for the treatment of skin inflammation diseases such as hidradenitis suppurativa (NCT06028230) and atopic dermatitis (NCT06058156). However, whether IRAK4 degraders exert beneficial effects in acute lung or other skin inflammatory diseases has not been explored.

In this study, we found that IRAK4 inhibition exerted a negligeable effect on NF-κB activation in lipopolysaccharide (LPS)-induced macrophages, which is mainly mediated by the nonenzymatic activity (scaffold function) of IRAK4. A new IRAK4 degrader, LC-MI-3, was rationally designed to efficiently eliminate both the kinase and scaffold functions of IRAK4, thereby enhancing its anti-inflammatory activity *in vitro* and *in vivo*. Our findings provide mechanistic insights into the relationship between inflammation and nonenzymatic

https://doi.org/10.1021/acs.jmedchem.4c00181
J. Med. Chem. 2024, 67, 8060−8076

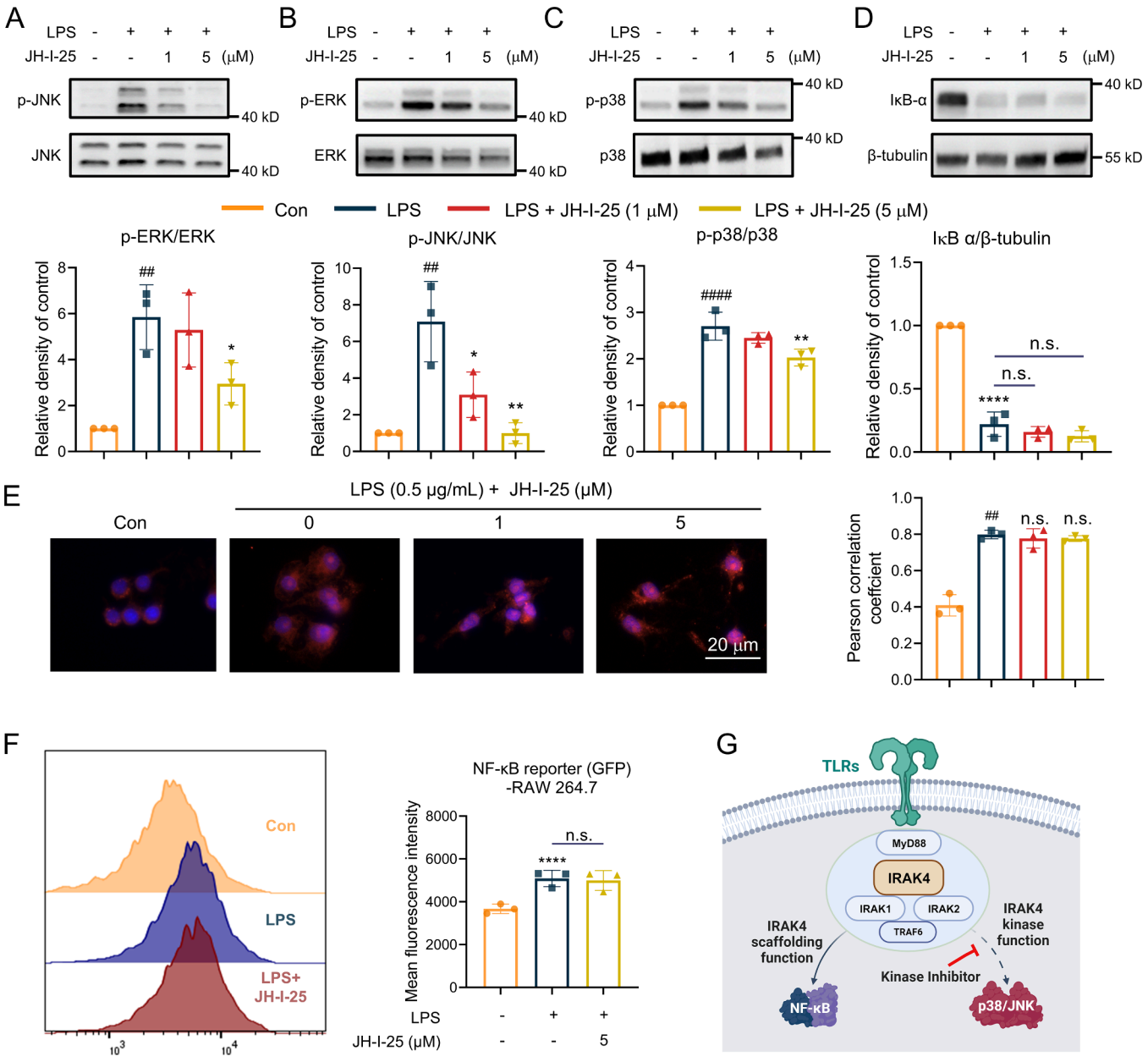

Figure 3. IRAK4 inhibitor exerts negligible effects on the scaffolding functions of IRAK4. (A–C) RAW264.7 cells were pretreated with JH-I-25 for 1 h and stimulated with 0.5 μg/mL lipopolysaccharide (LPS) for 2 h. Activation of the mitogen-activated protein kinase (MAPK) pathway determined by measuring the relative densities of (A) phospho-c-Jun N-terminal kinase (p-JNK), (B) phospho-extracellular signal-regulated kinase (p-ERK), and (C) p-p38. (D) Activation of the nuclear factor (NF)-κB pathway determined by measuring the relative density of IκB-α. (E) RAW264.7 cells were treated with JH-I-25, fixed, and stained with the p65 subunit (red) and 4′,6-diamidino-2-phenylindole (DAPI; blue). (F) Flow cytometry analysis of NF-κB pathway activation in RAW264.7-NF-κB-RE-EGFP cells. Cells were pretreated with JH-I-25 for 1 h and stimulated with 0.5 μg/mL LPS for 6 h. One-way analysis of variance (ANOVA) with Dunnett's posthoc test for multiple comparisons was used to analyze the differences in the means of LPS-induced, 1 μM JH-I-25-treated, and 5 μM JH-I-25-treated groups. $n = 3$ per group; mean ± standard deviation (SD). *$P < 0.05$, **$P < 0.01$, ***$P < 0.001$, and ****$P < 0.0001$; n.s. = not significant. G, IRAK4 kinase inhibitor block the kinase functions of IRAK4 but exert negligeable effects on Toll-like receptor (TLR)-mediated NF-κB activation.

activity of IRAK4. The identified degrader, LC-MI-3, can be used to interfere with the nonenzymatic activity of IRAK4 in both acute and chronic inflammatory diseases. To date, most PROTACs that have entered clinical trials were designed for cancer therapy and acted by degrading the androgen or estrogen receptor, or Bruton's tyrosine kinase.[27] Our study provides new evidence for degraders being used to treat nononcological diseases.

2. RESULTS

2.1. IRAK4 Inhibitor Exerts Negligeable Effects on the Scaffolding Functions of IRAK4. Previous studies have revealed the kinase and scaffold functions of IRAK4 in TLR signaling.[14] To identify the mechanisms underlying IRAK4 kinase inhibition, we examined its effects on TLR4 downstream signaling molecules. A previously developed IRAK4 inhibitor, JH-I-25[28] (Figure 1C), was used here to investigate and verify its effects on TLR4 downstream signaling pathways.

https://doi.org/10.1021/acs.jmedchem.4c00181
J. Med. Chem. 2024, 67, 8060−8076

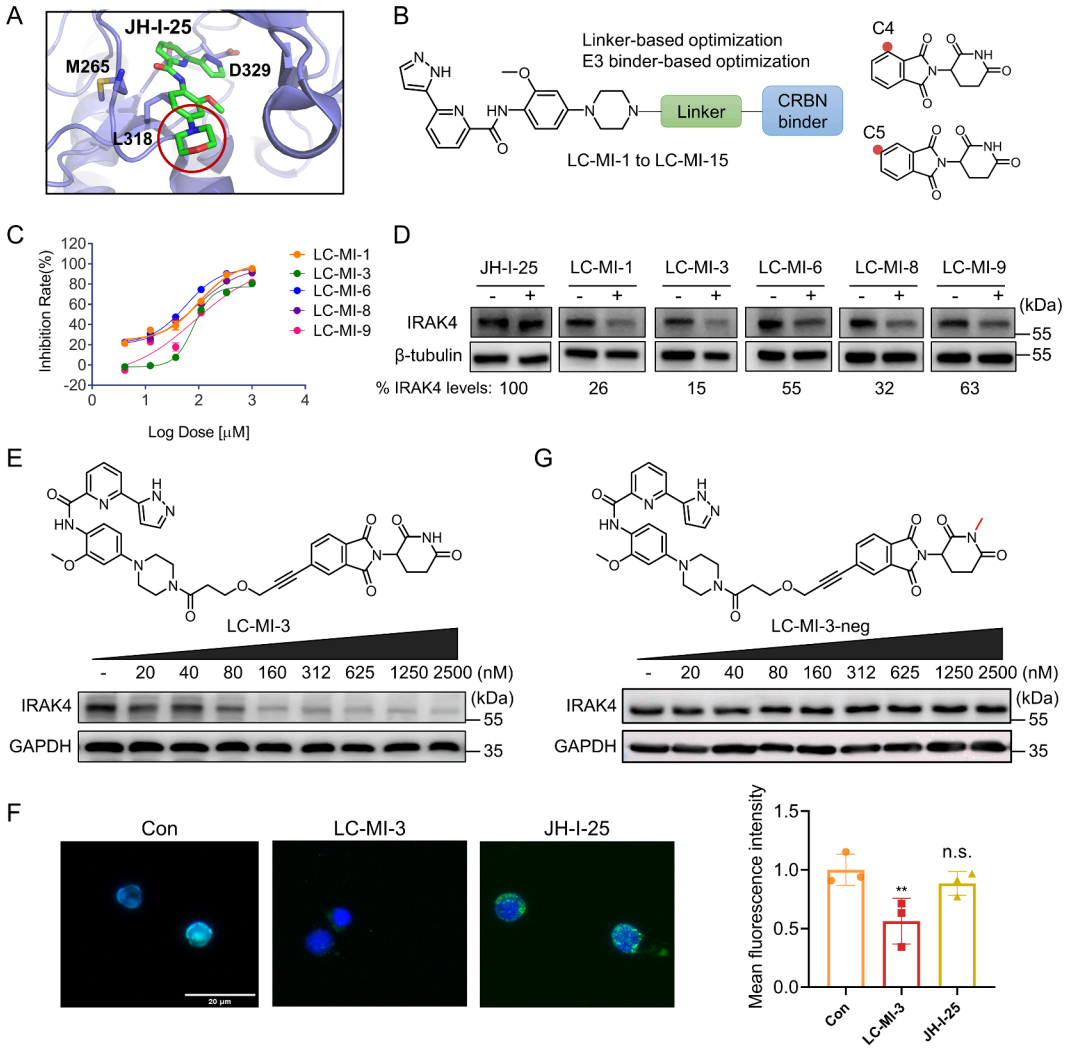

Figure 4. Identification of LC-MI-3 as an efficient IRAK4 degrader. (A) Structure of the JH-I-25−IRAK4 cocrystal and rationale of degrader design. (B) Degrader design strategy used in this study. (C) Kinase inhibitory activity of active compounds against IRAK4. (D) Representative blots showing the total IRAK4 levels in BaF3 cells stably expressing IRAK4 (BaF3-TEL-IRAK4) following treatment with compound JH-I-25 or indicated PROTACs at 100 nM for 12 h. (E) Chemical structure of degrader LC-MI-3. Western blotting of RAW264.7 cells treated with the indicated concentration of LC-MI-3 for 12 h. (F) Immunofluorescence assays of IRAK4 after treatment of peripheral blood mononuclear cells (PBMCs) with JH-I-25 or LC-MI-3 (100 nM). Scale bar, 50 μm. (G) Chemical structure of LC-MI-3-neg (negative control) and degradation potency evaluation.

RAW264.7 cells were pretreated with dimethyl sulfoxide (DMSO) or JH-I-25 (1 or 5 μM) and stimulated with LPS for 60 min to induce TLR4 activation. As shown in Figure 3A−C, RAW264.7 cells treated with JH-I-25 showed a significant loss of phospho-c-Jun N-terminal kinase (p-JNK), phospho-extracellular signal-regulated kinase (p-ERK), and p-p38. These results imply that IRAK4 inhibition attenuates LPS-induced mitogen-activated protein kinase (MAPK) activation. In contrast, JH-I-25 did not significantly affect the IκB-α levels after LPS stimulation (Figure 3D).

These observations suggests that TLR4-mediated NF-κB activation is independent of IRAK4 kinase activity. We next examined the NF-κB p65 nuclear translocation following JH-I-25 treatment. Similar to the degradation of IκB-α, IRAK4 kinase inhibition fail to reduce LPS-induced p65 translocation into the nucleus (Figure 3E). To further examine this, we generated NF-κB reporter macrophages. In RAW264.7 cells expressing the NF-κB−enhanced green fluorescence protein (EGFP) reporter, JH-I-25 pretreatment at 5 μM can hardly reduce the NF-κB activity induced by LPS compared to cells without JH-I-25 pretreatment (Figure 3F). Enzyme-linked immunosorbent assay (ELISA) demonstrated that the IRAK4 inhibitor, JH-I-25, had a modest anti-inflammatory effect (Figure S1). These results demonstrate that the inhibition of IRAK4 kinase activity by JH-I-25 has good MAPK inhibitory activity, which enables the inhibition of TLR cytokine production. However, JH-I-25 only had a negligible effect on the activation of NF-κB, as well as NF-κB p65 nuclear translocation. Thus, IRAK4 kinase activity is dispensable for LPS-TLR4-mediated NF-κB activation (Figure 3G).

2.2. Design and Optimization of IRAK4 Degraders.

PROTAC molecules consist of a specific POI binder, an E3 ligase recruiter, and a linker that tethers these two components in one molecule. To block the nonenzymatic functions of IRAK4, the compound JH-I-25 was chosen as an IRAK4 recruiter owing to its beneficial properties, such as good solubility and excellent *in vivo* exposure.[28] Analysis of the cocrystal structures of the type I JH-I-25 bound IRAK4 kinase

https://doi.org/10.1021/acs.jmedchem.4c00181
J. Med. Chem. 2024, 67, 8060−8076

Scheme 1

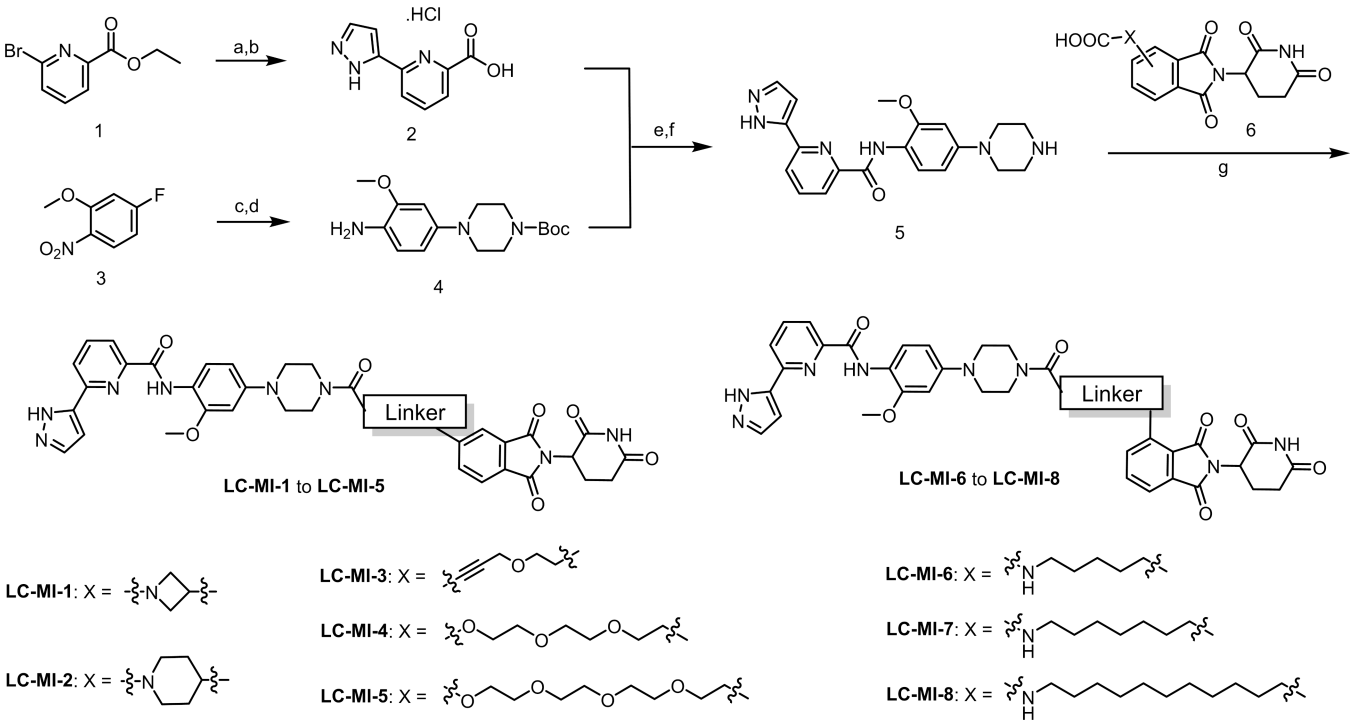

[a]Reagents and conditions: (a) 1-(tetrahydro-2*H*-pyran-2-yl)-5-(4,4,5,5-tetramethyl-1,3,2-dioxaborolan-2-yl)-1H-pyrazole, $Pd(dppf)Cl_2$, K_2CO_3, dioxane/H_2O, 90 °C, 12 h. (b) (i) NaOH, MeOH/H_2O, 1.5 h. (ii) HCl, ethyl acetate, 2 h. (c) *tert*-Butyl piperazine-1-carboxylate, K_2CO_3, DMF, 80 °C, overnight. (d) H_2, Pd/C, MeOH, rt, overnight. (e) HATU, TEA, DMF, rt, overnight. (f) HCl, ethyl acetate, rt, 2 h. (g) HATU, DIPEA, DMF, rt, 1 h.

Scheme 2

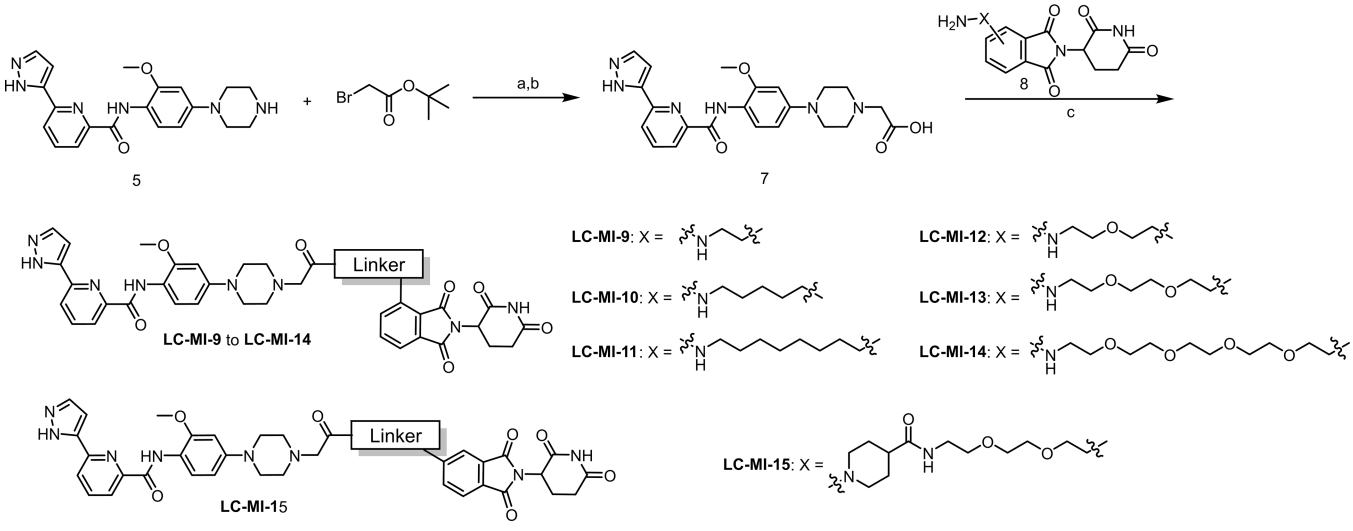

[a]Reagents and conditions: (a) K_2CO_3, DMF, rt, overnight. (b) TFA, DCM, rt, 2 h. (c) HATU, DIPEA, DMF, rt, 1 h.

region (PDB: 6EGE)[29] indicated that the morpholine ring was exposed to the solvent region; therefore, it could be utilized as a suitable linker attachment site (Figure 4A). The piperazine moiety was introduced as a replacement for morpholine to facilitate the conjugation of the linker (Figure 4B). Thalidomide was selected as the CRBN recruiter because of its successful application in the development of multiple degraders. Based on the crystal structures of thalidomide-bound DDB1-CRBN E3 ubiquitin ligase complex, the C4 and C5 positions of thalidomide are solvent-exposed and appropriate for linkage (Figure 4B).[30] To systematically investigated the linker length, composition, and linker binding sites, 15 CRBN-targeting chimeras were synthesized as novel candidate degraders. Previous studies have shown that amide condensation provides PROTAC synthesis with high yields and speed.[31−33] We utilized the exposed piperazine of JH-I-25 to perform a "forward" condensation with the exposed linker carboxyl, yielding eight bispecific compounds LC-MI-1−LC-

https://doi.org/10.1021/acs.jmedchem.4c00181
J. Med. Chem. 2024, 67, 8060−8076

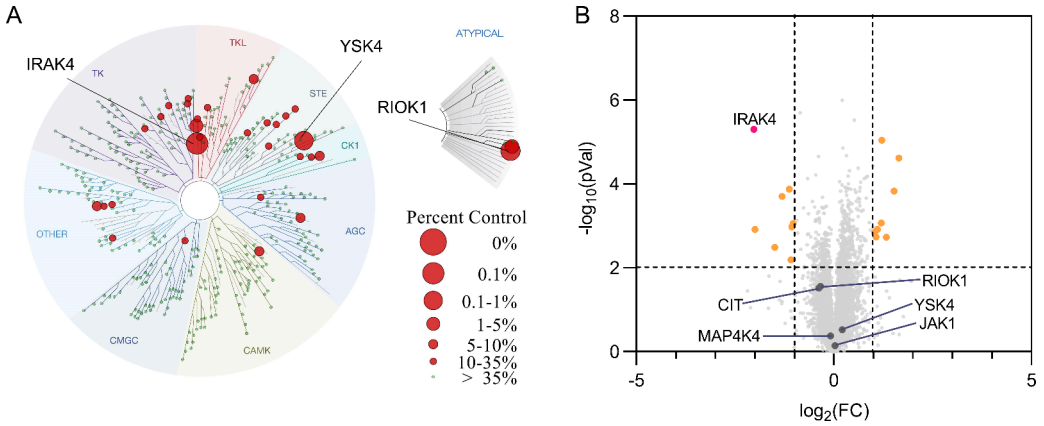

Figure 5. Target selectivity evaluation of LC-MI-3. (A) Selectivity profile of LC-MI-3 against a 486-kinase panel tested at a concentration of 1000 nM. Image was generated using the TREEspot Software (DiscoverX; Eurofins). (B) TMT-labeled proteomics analysis. RAW264.7 cells were treated with 200 nM LC-MI-3 for 12 h before proteomics measurement.

MI-8 (Scheme 1). Furthermore, to investigate whether the position of the amide bond affects the activities, we introduced acetic acid for "reverse" condensation, yielding seven bispecific compounds LC-MI-9−LC-MI-15 (Scheme 2).

2.3. Identification of LC-MI-3 as an Efficient IRAK4 Degrader. To determine the affinity of the synthesized compounds for IRAK4, all prepared molecules were subjected to IRAK4 kinase assays. As shown in Table S1, most of the designed molecules remained as potent biochemical inhibitors of IRAK4. In contrast, several chimeras, including LC-MI-2, 11, 14, and 15, showed decreased biochemical inhibition of IRAK4 kinase activity. This may be due to steric hindrance after the introduction of the CRBN ligands, which affects the binding ability of the warhead to the IRAK4 kinase domain. Five bivalent molecules (LC-MI-1, 3, 6, 8, and 9) those with IC_{50} values of <100 nM were selected to further evaluate the IRAK4 degrading potencies of IRAK4-expressing cells (Figure 4C).

As shown in Figure 4D, treatment with JH-I-25 or the five candidate degraders resulted in varying levels of IRAK4 degradation. Even though these chimeric compounds bind to the IRAK4 kinase domain, compound LC-MI-6 and LC-MI-9 did not translate into efficient IRAK4 degradation, with a degradation rate less than 50%. The degradation rate implies the percentage degradation observed after treatment with compounds at 100 nM compared to DMSO control. Thus, the chemical composition of linkers directly affected the degradation potency of designed PROTACs as reported in the case of other target classes.[34] It was shown that LC-MI-1 (IRAK4 IC_{50} = 166.1 nM), with azetidine as a linker, exhibited efficient IRAK4 protein degrading potential (degradation rate = 74%). Interestingly, as shown in Figure 4E, the introduction of a rigid alkynyl chain as conjunction linker yielded the most effective IRAK4 degrader, LC-MI-3 (IRAK4 IC_{50} = 57.2 nM), which reduced it by more than 80% (degradation rate = 85%). Compound LC-MI-3 displayed the dose-dependent IRAK4 degradation, with a half-maximal degradation concentration (DC_{50}) value of 47.38 nM in cells and a Dmax value of 91% (Figure 4E). In addition, immunofluorescence assays showed that LC-MI-3 significantly reduced the amount of intracellular IRAK4 in human peripheral blood mononuclear cells compared to that in the JH-I-25-treated group (Figure 4F). LC-MI-3 had no effect on the mRNA level of IRAK4 (Figure S2).

To verify that LC-MI-3-induced IRAK4 degradation occurred via the ubiquitin/proteasome system, a negative control compound, LC-MI-3-neg, was synthesized by integrating a methyl group into the crucial imide NH of the CRBN E3 ligase. The result indicated that the administration of LC-MI-3-neg failed to induce IRAK4 degradation (Figure 4G). To further investigate whether LC-MI-3-mediated IRAK4 degradation is proteasome-dependent, RAW264.7 cells were pretreated with the proteasome inhibitor MG-132 followed by a LC-MI-3 treatment. As shown in Figure S3, preincubation with MG132 markedly inhibited the LC-MI-3-induced reduction in IRAK4 levels. These results reveal that LC-MI-3-induced CRBN recruitment promoted IRAK4 ubiquitination and degradation. Enzymatic and cell-based results revealed that LC-MI-3 was the most effective degrader. Therefore, LC-MI-3 cells were selected for further studies.

2.4. Target Selectivity Evaluation of LC-MI-3. To explore target selectivity, we conducted kinome profile screening of LC-MI-3 against a panel of 468 kinases and disease-relevant mutated kinases at a test concentration of 1 μM. As shown in Figure 5A and Table S2, LC-MI-3 retained high binding affinity for IRAK4 (resulting in 99.8% inhibition of IRAK4). Next, we compared the profiling data of LC-MI-3 with those of its parent inhibitor, JH-I-25. Based the reported profile data of JH-I-25, eight kinases were found with inhibition rate above 95% except IRAKs, including YSK4, MAP4K4, MEK5, CIT, JAK1/3, RIOK1, and TNIK.[29] In contrast, among the 468 kinases (except IRAK4), only three kinases were identified for LC-MI-3 (RIOK1/3, IRAK1, and YSK4) with inhibition rates greater than 95%. Notably, among tyrosine kinase (TK) and tyrosine kinase-like (TKL) families, IRAK4 is the only kinase significantly inhibited by LC-MI-3. The selectivity variation between LC-MI-3 and the lead compound JH-I-25 may be due to steric interference between the linker and the E3 ligase recruiting moiety of LC-MI-3 with kinase, thus destabilizing the binary complexes.

To further test the target selectivity of LC-MI-3 in cells, TMT-labeled quantitative proteomic analysis was performed on RAW264.7 cells. The results indicated that IRAK4 was the major target downregulated after treatment with LC-MI-3 for 12 h, demonstrating the selectivity of LC-MI-3 for IRAK4 (Figure 5B). In addition, Western blotting results indicated that RIOK1 and immunomodulatory imide drug-dependent substrates, including IKZF1, IKZF3, and SALL4, were not

https://doi.org/10.1021/acs.jmedchem.4c00181
J. Med. Chem. 2024, 67, 8060−8076

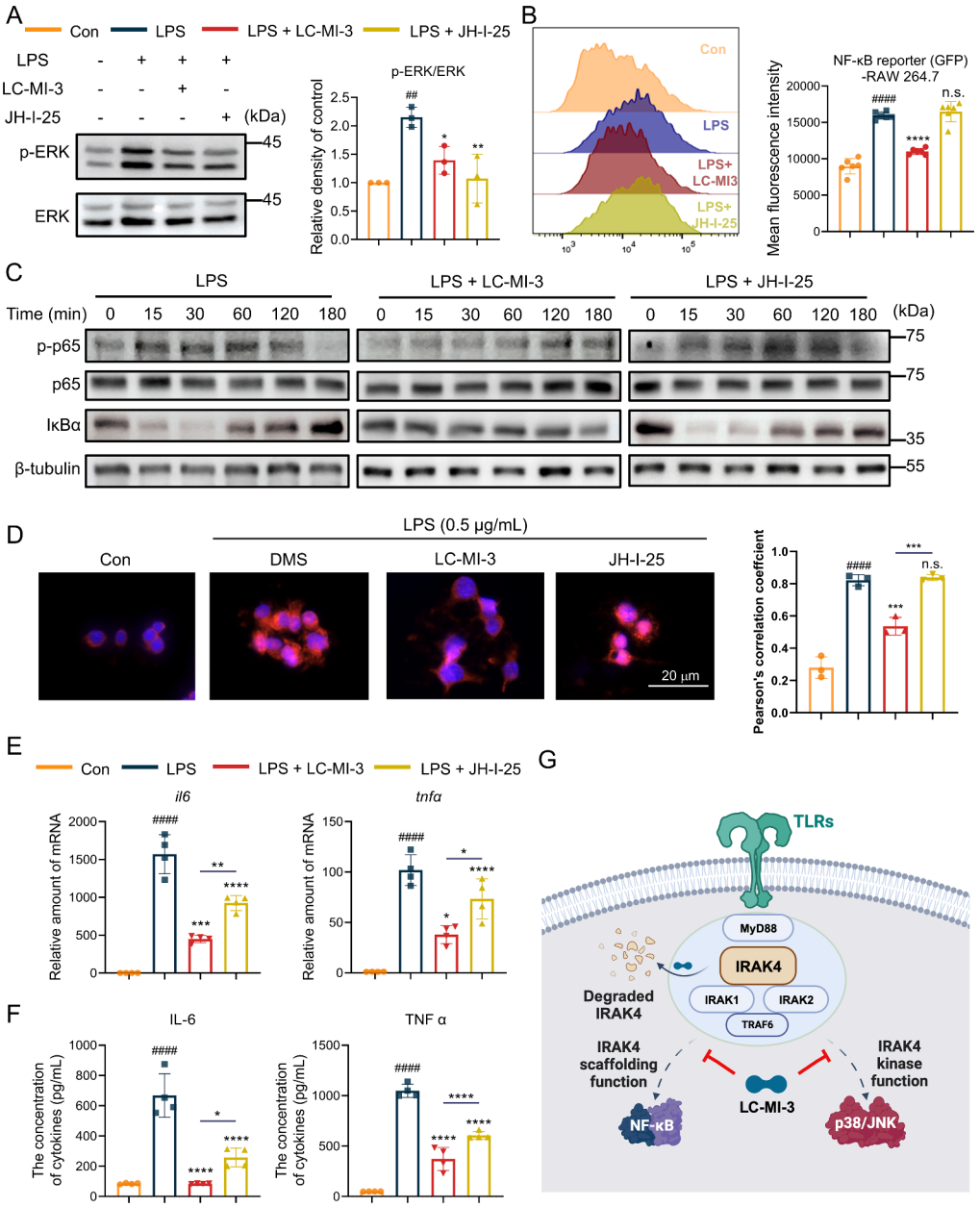

Figure 6. LC-MI-3 blocks both the kinase and scaffolding functions of IRAK4. (A) Immunoblotting analysis of ERK activation in RAW264.7 cells pretreated with 1 μM LC-MI-3 and JH-I-25 for 1 h and stimulated with 0.5 μg/mL LPS for 2 h. (B) Flow cytometry analysis of NF-κB pathway activation in RAW264.7-NF-κB-RE-EGFP cells. Cells were pretreated with 1 μM LC-MI-3 and JH-I-25 for 1 h and stimulated with 0.5 μg/mL LPS for 6 h. (C) Immunoblotting analysis of NF-κB pathway activation in RAW264.7 cells pretreated with 1 μM LC-MI-3 and JH-I-25 for 1 h and stimulated with 0.5 μg/mL LPS for 15, 30, 60, 120, and 180 min. (D) RAW264.7 cells were treated as panel B, fixed, and stained with p65 subunit (red) and DAPI (blue). (E) Real-time polymerase chain reaction (PCR) analysis of *il6* and *tnfα* levels in the RAW264.7 cell lysate. (F) Enzyme-linked immunosorbent assay (ELISA) of IL-6 and TNF-α levels in RAW264.7 cells treated as panel B. (G) Action mechanism of LC-MI-3 and its potential advantage over the IRAK4 kinase inhibitor, JH-I-25, in the inhibition of TLR-driven inflammatory signaling by blocking the scaffolding and kinase functions of IRAK4. One-way ANOVA with Dunnett's posthoc test for multiple comparisons of differences in the means of LPS-induced, LC-MI-3-treated, and JH-I-25-treated groups. n = 3 per group; mean ± SD; *P < 0.05, **P < 0.01, ***P < 0.001, and ****P < 0.0001; n.s. = not significant.

degraded by LC-MI-3 (Figure S4). Therefore, LC-MI-3 showed a high degree of selectivity against IRAK4 and increased target selectivity compared to its parent inhibitor.

2.5. LC-MI-3 Blocks Both the Kinase and Scaffolding Functions of IRAK4. We have demonstrated that inhibition of IRAK4 by JH-I-25 can prevent MyD88-dependent MAPK activation, while barely inhibiting LPS-induced NF-κB activation. As shown in Figure 6A, both LC-MI-3 and JH-I-25 potently inhibited MAPK phosphorylation in RAW264.7 cells. We further evaluated whether degrader LC-MI-3 could suppress the NF-κB and downstream inflammatory signaling pathways. Compared to JH-I-25, LC-MI-3 treatment can significantly reduce the NF-κB activity in LPS challenged RAW264.7 cells expressing NF-κB−EGFP reporter (Figure 6B). Upon stimulation by LPS, the phosphorylation of NF-κB p65 was increased as early as 15 min (Figure 6C). LC-MI-3

https://doi.org/10.1021/acs.jmedchem.4c00181
J. Med. Chem. 2024, 67, 8060−8076

Table 1. *In Vivo* Pharmacokinetic Properties of LC-MI-3

Parameter	$T_{1/2}$ (h)	T_{max} (h)	C_{max} ng/mL	$AUC_{(0-\infty)}$ h·ng/mL	V_{ss} mL/kg	CL mL/h/kg	F (%)
i.v. (2 mg/kg)	0.486	0.083	2915.6	1327.1	583.5	1534.8	
p.o. (20 mg/kg)	1.453	0.500	440.2	1077.9			8.15

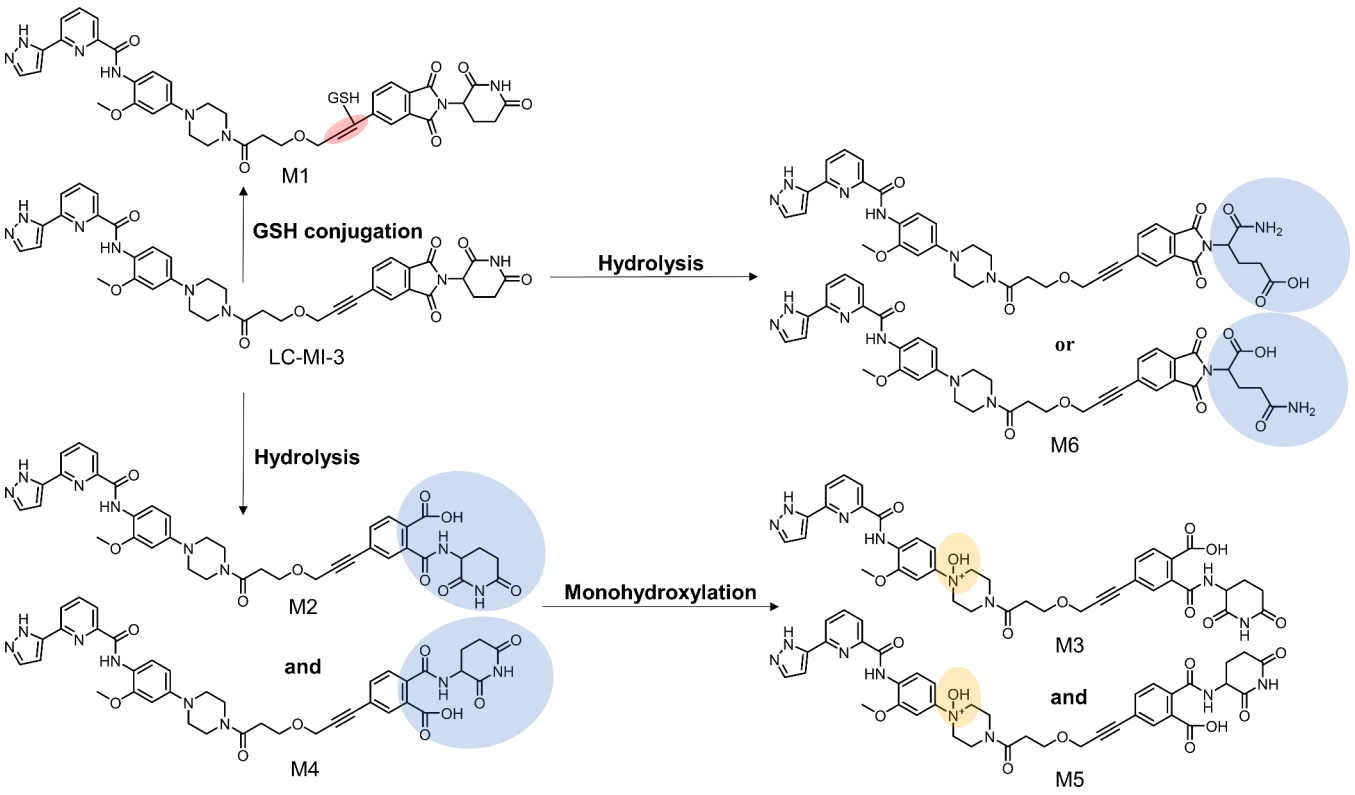

Figure 7. Proposed metabolic pathways of LC-MI-3.

blocked the phosphorylation of NF-κB p65 and showed complete inhibition of IκB-α degradation. In contrast, IκB-α degradation occurred as early as 15 min in JH-I-25-treated macrophages (Figure 6C). In addition, LC-MI-3 treatment significantly reduced LPS-induced p65 translocation into the nucleus compared to JH-I-25 treatment (Figure 6D). Compared to the parent inhibitor, LC-MI-3 treatment showed a significantly higher potency to normalize LPS-induced interleukin-6 (IL-6) and tumor necrosis factor α (TNFα) mRNA expression as well as cytokine production in macrophages (Figure 6E−F and Figure S5).

Previous studies have shown that LPS stimulation increases TLR4 endocytosis, which initiates downstream signaling pathways. IRAK4 was found to be involved in TLR4 endocytosis.[35] Thus, we studied the effect of LC-MI-3 on the endocytosis of cell membrane-bound TLR4. As shown in Figure S6, LPS-stimulated macrophages showed significantly elevated receptor endocytosis, as determined by flow cytometry. Interestingly, similar endocytosis levels were observed in the LPS-stimulated control and JH-I-25-treated group, whereas LC-MI-3-treated cells showed a slight decrease in endocytosis. This result was in line with that of a previous study showing that *Irak4*$^{-/-}$ bone marrow derived macrophages (BMDM) exhibited decreased endocytosis compared to macrophages expressing kinase-deficient IRAK4.[15] Together, these results confirmed that the removal of both the kinase and scaffolding functions of IRAK4 via LC-MI-3 may lead to superior and broader potency than that of kinase inhibitors in inhibiting LPS-induced inflammation.

2.6. LC-MI-3 Is an Orally Efficacious IRAK4 Degrader.

To evaluate its practicability *in vivo*, we investigated the PK profile of LC-MI-3 in mice (Table 1). Plasma concentrations of LC-MI-3 were determined following a single-dose treatment of LC-MI-3 via intravenous injection (i.v., 2 mg/kg) or oral administration (p.o., 20 mg/kg). LC-MI-3 exhibited rapid absorption after oral administration, with the Cmax being reached at 1.5 h. Acceptable plasma concentrations of LC-MI-3 were detected during the course of the experiment. LC-MI-3 is orally bioavailable with $F = 8.1 \pm 2.7\%$.

We investigated the metabolite profile of LC-MI-3 in rat hepatocytes. Under these experimental conditions, six metabolites (M1-M6) were detected in hepatocytes samples (Figure S7). The biotransformation of LC-MI-3 mainly involves glutathione conjugation, hydrolysis, and hydroxylation. The major metabolite, M1, was formed via glutathione conjugation to the alkynyl moiety of LC-MI-3. Based on the metabolite profiling data, five metabolites were generated by amide hydrolysis (M2, M4, and M6), followed by monohydroxylation (M3 and M5). The chemical structures of the six identified metabolites and their potential metabolic pathways are shown in Figure 7. Based on the metabolite information, we found that the IRAK4 binding part of LC-MI-3 was relatively stable, whereas the CRBN ligand and alkynyl part were likely to form a reaction via glutathione conjugation and hydrolysis in hepatocytes. Further studies on LC-MI-3 should

https://doi.org/10.1021/acs.jmedchem.4c00181
J. Med. Chem. 2024, 67, 8060−8076

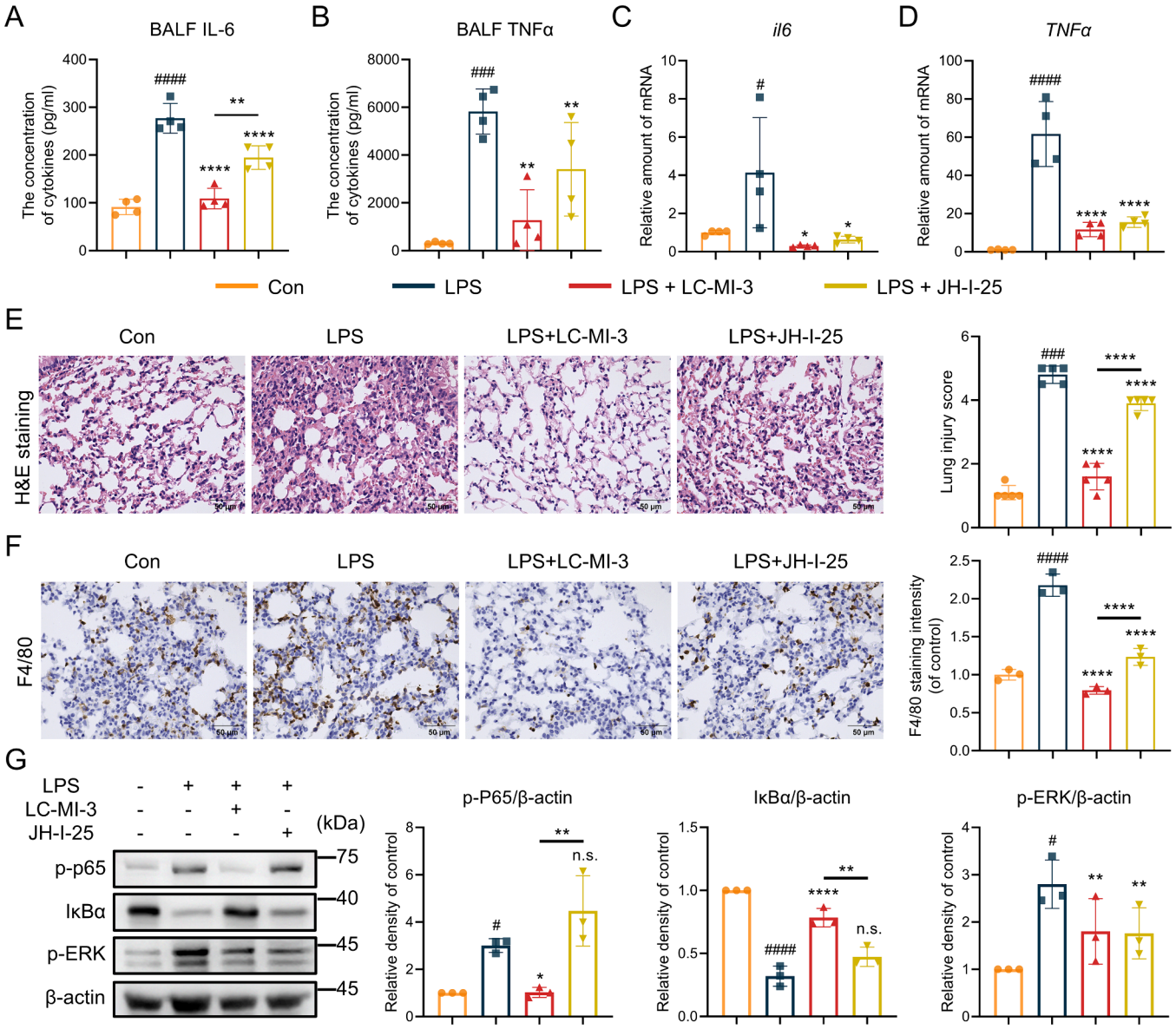

Figure 8. LC-MI-3 suppresses lung injury in the LPS-induced mouse ALI model. (A, B) C57BL/6 mice were pretreated with 20 mg/kg LC-MI-3, JH-I-25, or saline and stimulated with 5 mg/kg LPS for 6 h. IL-6 and TNF-α levels in bronchoalveolar lavage fluid (BALF) were analyzed using ELISA. (C, D) Real-time PCR analysis of *il6* and *tnfα* levels in serum. (E) Hematoxylin and eosin (H&E) staining and (F) F4/80 immunohistochemical analysis of the lung tissues. (G) Representative immunoblots and density analysis of p-p65, IκB-α, and p-ERK levels in the lung tissues. One-way ANOVA with Dunnett's posthoc test for multiple comparisons of differences in the means of LPS-induced, LC-MI-3-treated, and JH-I-25-treated groups. $n = 3$ per group; mean ± SD; $^{*}P < 0.05$, $^{**}P < 0.01$, $^{***}P < 0.001$, and $^{****}P < 0.0001$; n.s. = not significant.

focus on improving its bioavailability by exploring novel cereblon ligands with improved oral bioavailability.[36]

2.7. Protective Effects of LC-MI-3 on LPS-Induced ALI in Mice. The good anti-inflammatory activity, high kinome selectivity, and oral bioavailability of LC-MI-3 suggest that it is a promising candidate compound for use in IRAK4-driven inflammation models *in vivo*. Previous preclinical data have provided proof-of-concept that IRAK4 is a promising therapeutic target for treating inflammatory lung diseases. We assessed the anti-inflammatory effects of LC-MI-3 in an animal model of LPS-induced ALI. C57BL/6 mice were treated with 10 mg/kg LC-MI-3 before the LPS challenge. The parental IRAK4 kinase inhibitor JH-I-25 was used as a positive control. The bronchoalveolar lavage fluid (BALF) of mice was harvested following intratracheal administration of low-dose LPS (5 mg/kg). As shown in Figure 8A–B, the induction of pro-inflammatory cytokines (TNF-α and IL-6) in BALF in response to LPS was significantly reduced in mice treated with LC-MI-3. In addition, the transcript levels of TNF-α and IL-6 in the lung tissues were inhibited by LC-MI-3 treatment, with the *Il6* level in particular significantly lowered to the control level (Figure 8C–D).

Histological analysis of the lung sections revealed that LC-MI-3 prevented the structural disruption of lung tissue in response to LPS (Figure 8E). To further evaluate whether LC-MI-3 prevents macrophage infiltration in the LPS-induced ALI model, we performed an immunohistochemical analysis of F4/80 (a macrophage marker). Immunohistochemical staining data showed increased F4/80 immunoreactivity in the lung tissues of LPS-challenged mice, whereas F4/80-positive

https://doi.org/10.1021/acs.jmedchem.4c00181
J. Med. Chem. 2024, 67, 8060−8076

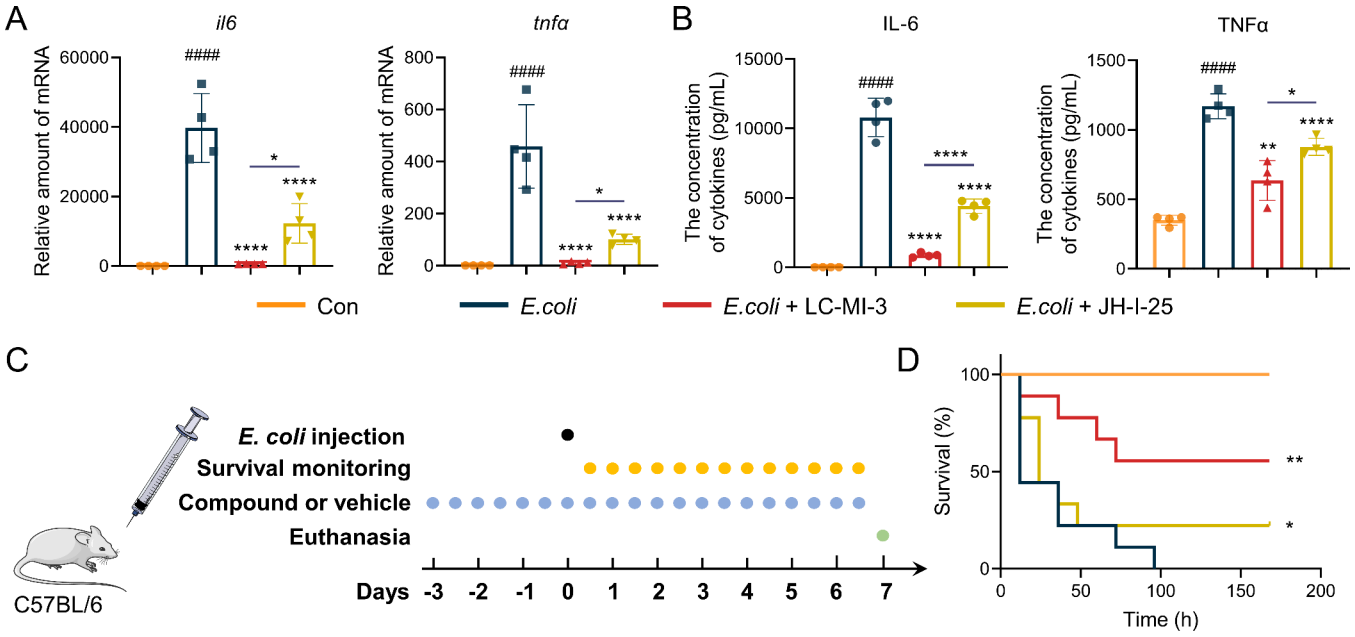

Figure 9. LC-MI-3 attenuates *Escherichia coli*-induced inflammatory reaction and sepsis. (A) Real-time PCR analysis of *il6* and *tnfα* levels in the RAW264.7 cell lysate. Cells were pretreated with 1 μM LC-MI-3 or JH-I-25 for 6 h and stimulated with 10^{10} CFU/mL *E. coli* for 6 h. n = 4 per group; mean ± SD (B) ELISA of IL-6 and TNF-α levels in the RAW264.7 cell culture medium treated as panel A. n = 3 per group; mean ± SD. One-way ANOVA with Dunnett's posthoc test for multiple comparisons of differences in the means of *E. coli*-induced, LC-MI-3-treated, and JH-I-25-treated groups in panels A and B. (C) C57BL/6 mice were pretreated with 20 mg/kg JH-I-25, LC-MI-3, or vehicle via intragastric injections twice a day from 3 days before *E. coli* injection to the end of the experimental period. The survival of mice was monitored every 12 h after injection. (D) Survival curves of mice treated as panel C. Kaplan−Meier survival curves were used for analysis. n = 8 per group. *P < 0.05, **P < 0.01, ***P < 0.001, and ****P < 0.0001; n.s. = not significant.

macrophages were significantly decreased in LC-MI-3-treated mice compared to the control and JH-I-25-treated group (Figure 8F).

We further assessed the effects of LC-MI-3 on the downstream MAPK and NF-κB activities *in vivo*. Immunoblotting analysis of mice lung tissue samples showed that LPS challenge induced the phosphorylation of both p65 and ERK and reduced the IκB-α levels (Figure 8G). JH-I-25 exhibited good MAPK inhibition activity *in vivo* as confirmed by the significantly reduced p-ERK levels, whereas JH-I-25 only exhibited a weak inhibition activity on IκB-α degradation. Similar to the *in vitro* studies, LC-MI-3 exhibited superior inhibition activity against NF-κB compared to the kinase inhibitor, JH-I-25.

2.8. LC-MI-3 Protects the Mice against LPS-Induced Septic Death. IRAK4 scaffold is essential for the host response to Gram-negative bacteria.[15] Hence, IRAK4 deficiency may protect mice against bacteria-induced septic death. To investigate whether the results observed with purified LPS correlate with responses to live bacteria, we conducted infection assays in RAW264.7 cells using *Escherichia coli*. In macrophages infected with *E. coli*, LC-MI-3 suppressed the transcription and production of inflammatory cytokines better than JH-I-25 (Figure 9A and B). Next, we assessed the effects of LC-MI-3 on mice infected with intraperitoneal *E. coli in vivo*. As shown in Figure 9C and D, mice treated with LPS alone died within 100 h, whereas those treated with LC-MI-3 showed significantly increased survival compared to those treated with JH-I-25. Collectively, our data suggest that LC-MI-3 induces IRAK4 scaffold deficiency, which impairs the host response to Gram-negative bacteria.

2.9. LC-MI-3 Exerts Robust Therapeutic Effects in the TLR7-Driven Psoriasis Model. IRAK4 is an essential player in skin inflammatory processes and acts as a potential therapeutic target for chronic inflammatory skin diseases.[5] As the scaffold function of IRAK4 is essential for both TLR4-mediated inflammatory and TLR7 signaling pathways,[37] we assessed the therapeutic effects of LC-MI-3 in a mouse model of psoriasis induced by imiquimod (IMQ). Dexamethasone (Dex) was used as the positive control. As shown in Figure 10A, LC-MI-3-treated group exhibited a greater improvement in the clinical signs of psoriasis, including IMQ-induced swelling, scaling, and erythema scores, after 6 days of treatment compared to the JH-I-25-treated group (Figure 10B−C and Figure S8). Furthermore, keratinocyte proliferation, epidermal acanthosis, mastoid processes, and dermal inflammatory cell infiltration were significantly attenuated following LC-MI-3 treatment (Figure 10D and E). LC-MI-3 treatment also inhibited the increase in spleen weight and skin thickness (Figure 10F−G). Notably, no difference in body weight was observed between the vehicle- and LC-MI-3-treated groups (Figure 10H).

3. DISCUSSION AND CONCLUSIONS

IRAK4 is the most upstream kinase involved in IL-1R and TLR signaling. IRAK4 functions in a MyD88-dependent pathway and has great therapeutic importance in anti-inflammatory and anticancer drug development. Various IRAK4 inhibitors have been evaluated in clinical trials. However, inhibition of IRAK4 kinase activity alone may not be sufficient for therapy because IRAK4 acts as both a scaffolding protein and an active kinase. Moreover, IRAK4 kinase activity may not be disease-specific in certain contexts. Therefore, eliminating both the scaffolding

https://doi.org/10.1021/acs.jmedchem.4c00181
J. Med. Chem. 2024, 67, 8060−8076

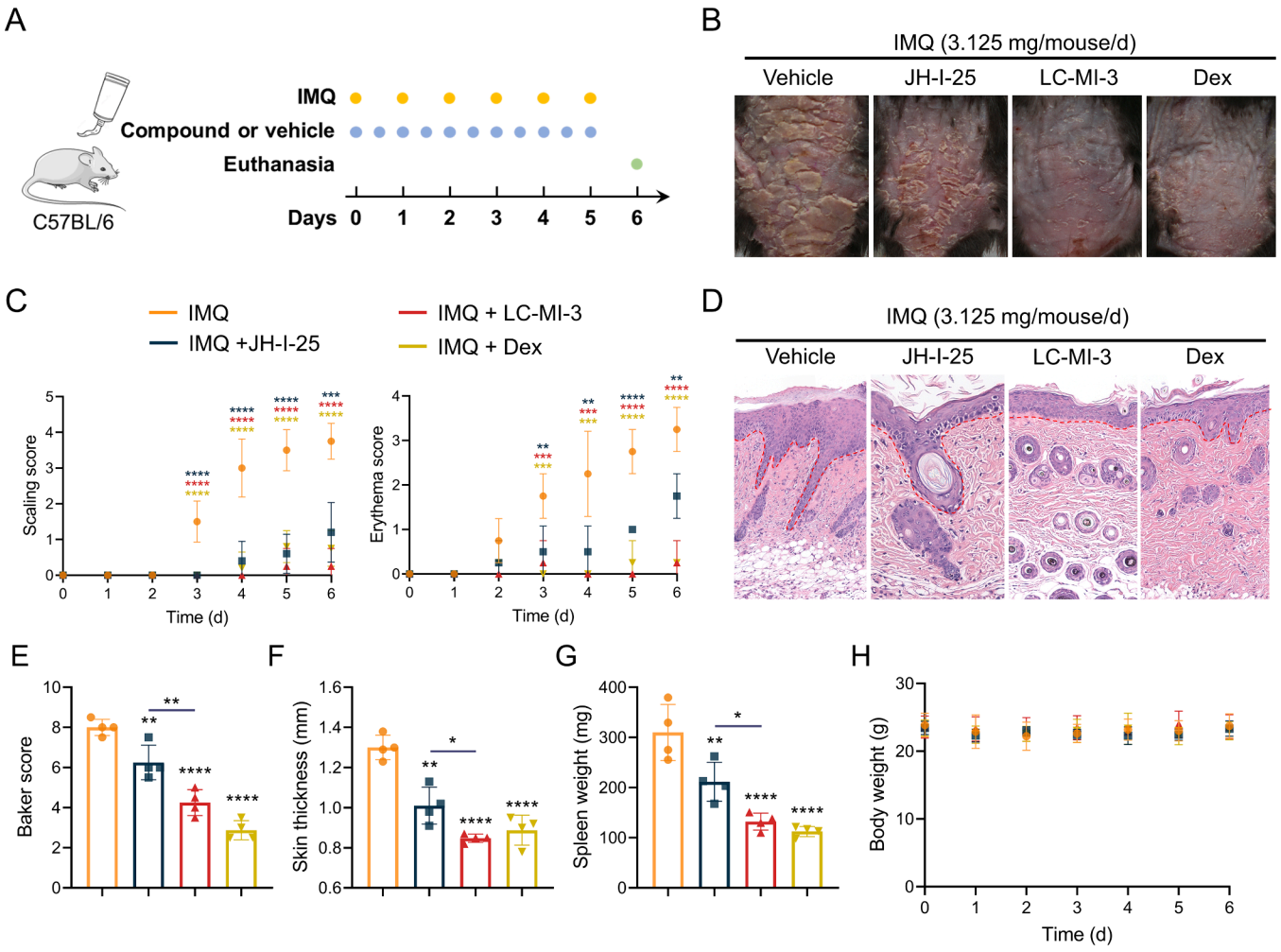

Figure 10. LC-MI-3 suppresses the TLR7-mediated inflammatory reaction. (A) C57BL/6 mice was were treated with 20 mg/kg JH-I-25 or LC-MI-3 or 3 mg/kg dexamethasone (Dex) twice a day, and 3.125 mg/mouse imiquimod (IMQ) cream was applied on the shaved back region of the mice daily. (B) Representative images of the mouse back skin on day 6. (C) Scaling and erythema were evaluated daily. (D, E) H&E staining (D) and Baker score evaluation (E) of the mouse back skin. (F, G) Thickness of the back skin (F) and spleen weight (G) measured on day 7. (H) Body weight of mice monitored daily. n = 4 per group; mean ± SD; *P < 0.05, **P < 0.01, ***P < 0.001, and ****P < 0.0001; n.s. = not significant.

and kinase functions of IRAK4 may enhance the therapeutic efficacy.

Although several IRAK4 degraders have been developed, they have not shown promising results in IRAK4-related acute inflammation or skin inflammatory diseases. In this study, we report a small-molecule IRAK4 degrader, LC-MI-3, which potently degrades the intracellular kinase protein, IRAK4. LC-MI-3 effectively reduced the IRAK4 protein levels in cells and exhibited strong anti-inflammatory activity *in vitro* compared to the traditional kinase inhibitors. Among the 468 kinases tested in this study, LC-MI-3 demonstrated excellent target selectivity for IRAK4 and acceptable oral bioavailability in mice. Our results revealed the role of the IRAK4 degrader, LC-MI-3, in the development of TLR-driven inflammatory diseases and showed its robust and potent *in vivo* activity in a mouse model of TLR4-mediated ALI and sepsis and TLR7-mediated psoriasis.

Collectively, our results suggest that eliminating both the kinase and scaffolding functions of IRAK4 can enhance its therapeutic effects better than the inhibition of kinase activity alone. Our data also suggest LC-MI-3 as a highly promising candidate for the treatment of TLR-mediated acute inflammatory diseases, inflammatory skin diseases, and TLR/IRAK4-dependent oncological diseases. A limitation of this study is the relatively low bioavailability of LC-MI-3 due to the characteristics of heterobifunctional degraders. Future efforts are required to improve bioavailability and investigate whether the beneficial anti-inflammatory effect of LC-MI-3 observed in animal models corresponds to similar clinical results.

4. EXPERIMENTAL SECTION

4.1. Chemistry. All target compounds were purified via column chromatography with an elution system of DCM and methanol in different ratios, and their structures were confirmed via ^{1}H nuclear magnetic resonance (NMR), ^{13}C NMR, and liquid chromatograph–mass spectrometry (LC-MS). High-resolution MS data were recorded using an Agilent 6520 accurate mass Q-TOF LC/MS system (1200e6520; Agilent). ^{1}H and ^{13}C NMR spectral data were recorded on a 400 MHz spectrometer (Bruker Magnet System 400' 54 Ascend). Unless otherwise stated, all solvents or reagents were obtained from commercially available materials and used directly without further purification. Column chromatography was performed using a 200–300 mesh silica gel. The purities of all the synthesized compounds were >95% determined using the analytical HPLC on a Shimadzu LC-20AD system, Diamonsil C18 column.

4.1.1. N-(4-(4-(3-((3-(2-(2,6-Dioxopiperidin-3-yl)-1,3-dioxoisoindolin-5-yl)prop-2-yn-1-yl)oxy)propanoyl)piperazin-1-yl)-2-methox-

https://doi.org/10.1021/acs.jmedchem.4c00181
J. Med. Chem. 2024, 67, 8060–8076

yphenyl)-6-(1H-pyrazol-5-yl)picolinamide (LC-MI-3). N-(2-methoxy-4-(piperazin-1-yl)phenyl)-6-(1H-pyrazol-5-yl)picolinamide (5) (50 mg, 0.13 mmol), 3-((3-(2-(2,6-dioxopiperidin-3-yl)-1,3-dioxoisoindolin-5-yl)prop-2-yn-1-yl)oxy)propanoic acid (51 mg, 0.13 mmol), HATU (53 mg, 0.14 mmol), DIPEA (113 μL, 0.65 mmol) were dissolved in and 2 mL DMF. The reaction was stirred for 1h and diluted with H_2O. After extraction, the combined organic layer was concentrated and purified by chromatography on silica gel (DCM/MeOH 50:1) to yield the target compound: yellow powder (62 mg, 64%). ^{1}H NMR (400 MHz, DMSO-d_6) δ 13.23 (s, 1H), 11.14 (s, 1H), 10.58 (s, 1H), 8.21 (s, 2H), 8.14−8.00 (m, 2H), 7.93 (d, J = 9.6 Hz, 4H), 6.99 (s, 1H), 6.75 (s, 1H), 6.56 (dd, J = 8.9, 2.5 Hz, 1H), 5.16 (dd, J = 12.9, 5.4 Hz, 1H), 4.47 (s, 2H), 3.98 (s, 3H), 3.83 (t, J = 6.4 Hz, 2H), 3.68−3.57 (m, 5H), 3.17 (d, J = 24.0 Hz, 5H), 2.72 (t, J = 6.5 Hz, 2H), 2.63−2.51 (m, 2H). ^{13}C NMR (100 MHz, DMSO) δ 173.20, 170.20, 169.14, 166.90, 166.81, 138.05, 132.24, 131.01, 128.70, 126.24, 124.26, 91.36, 84.58, 66.54, 58.52, 49.60, 45.32, 41.39, 40.61, 40.40, 40.19, 39.98, 39.77, 39.56, 39.35, 33.04, 31.37, 22.39. LC-MS (ESI$^+$): calcd for $C_{39}H_{36}N_8O_8$ 744.27, found, 767.30 [M + Na]$^+$, 745.50 [M + H]$^+$. HPLC t_R = 12.549 min (95.41% purity).

4.1.2. N-(2-Methoxy-4-(4-(3-((3-(2-(1-methyl-2,6-dioxopiperidin-3-yl)-1,3-dioxoisoindolin-5-yl)prop-2-yn-1-yl)oxy)propanoyl)-piperazin-1-yl)phenyl)-6-(1H-pyrazol-5-yl)picolinamide (LC-MI-3 Neg). Bispecific compound LC-MB-3 Neg was synthesized in a similar manner as bispecific compound LC-MI-3, yellow powder (52%). ^{1}H NMR (400 MHz, Chloroform-d) δ 10.46 (s, 1H), 8.37 (d, J = 8.6 Hz, 1H), 8.16 (d, J = 7.5 Hz, 1H), 8.00−7.86 (m, 2H), 7.84 (s, 1H), 7.75−7.63 (m, 3H), 6.93 (s, 1H), 6.56−6.44 (m, 2H), 5.05−4.96 (m, 1H), 4.41 (s, 2H), 3.94 (t, J = 6.3 Hz, 2H), 3.88 (s, 3H), 3.85−3.77 (m, 2H), 3.71−3.64 (m, 2H), 3.17 (s, 5H), 3.15−3.08 (m, 2H), 3.02−2.60 (m, 6H). ^{13}C NMR (100 MHz, $CDCl_3$) δ 171.15, 169.34, 168.64, 166.87, 166.71, 161.43, 149.93, 149.87, 148.88, 147.96, 138.50, 137.50, 131.92, 130.71, 129.21, 126.62, 123.72, 122.40, 121.30, 121.19, 120.76, 108.77, 104.00, 100.66, 90.21, 84.59, 77.43, 77.11, 76.79, 66.84, 59.14, 56.05, 50.64, 50.29, 49.95, 45.74, 41.61, 33.53, 31.87, 29.72, 27.30, 21.95, 14.15. LC-MS (ESI$^+$): calcd for $C_{40}H_{38}N_8O_8$ 758.3, found, 759.2 [M + H]$^+$, 781.2 [M + Na]$^+$.

4.1.3. N-(4-(4-(1-(2-(2,6-Dioxopiperidin-3-yl)-1,3-dioxoisoindolin-5-yl)azetidine-3-carbonyl)piperazin-1-yl)-2-methoxyphenyl)-6-(1H-pyrazol-5-yl)picolinamide (LC-MI-1). Yellow-green powder (43%). ^{1}H NMR (400 MHz, DMSO-d_6) δ 13.23 (s, 1H), 11.08 (s, 1H), 10.58 (s, 1H), 8.17 (s, 2H), 8.10 (t, J = 7.6 Hz, 1H), 8.04 (dd, J = 7.3, 1.4 Hz, 1H), 7.90 (s, 1H), 7.66 (d, J = 8.2 Hz, 1H), 6.99 (d, J = 2.2 Hz, 1H), 6.85 (d, J = 2.1 Hz, 1H), 6.79 (d, J = 2.5 Hz, 1H), 6.71 (dd, J = 8.4, 2.1 Hz, 1H), 6.60 (dd, J = 8.8, 2.5 Hz, 1H), 5.06 (dd, J = 12.9, 5.4 Hz, 1H), 4.27 (t, J = 8.5 Hz, 2H), 4.22−4.14 (m, 2H), 4.04−3.93 (m, 5H), 3.68 (t, J = 5.1 Hz, 2H), 3.51 (t, J = 5.1 Hz, 2H), 3.24−3.15 (m, 5H), 2.63−2.51 (m, 2H). ^{13}C NMR (100 MHz, DMSO) δ 173.29, 170.58, 169.79, 167.91, 167.64, 155.45, 134.26, 125.30, 117.69, 105.05, 100.97, 54.11, 49.19, 40.58, 40.37, 40.16, 39.95, 39.74, 39.53, 39.32, 31.69, 31.43. LC-MS (ESI$^+$): calcd for $C_{37}H_{35}N_9O_7$ 717.27, found, 740.24 [M + Na]$^+$, 718.31 [M + H]$^+$. HPLC t_R = 12.331 min (99.11% purity).

4.1.4. N-(4-(4-(1-(2-(2,6-Dioxopiperidin-3-yl)-1,3-dioxoisoindolin-5-yl)piperidine-4-carbonyl)piperazin-1-yl)-2-methoxyphenyl)-6-(1H-pyrazol-5-yl)picolinamide (LC-MI-2). Yellow powder (63%). ^{1}H NMR (400 MHz, DMSO-d_6) δ 13.24 (s, 1H), 11.09 (s, 1H), 10.61 (s, 1H), 8.27 (d, J = 8.7 Hz, 1H), 8.20 (d, J = 7.8 Hz, 1H), 8.14−8.01 (m, 2H), 7.96−7.92 (m, 1H), 7.67 (d, J = 8.5 Hz, 1H), 7.34 (d, J = 2.2 Hz, 1H), 7.25 (dd, J = 8.8, 2.2 Hz, 1H), 7.02−6.97 (m, 1H), 6.79 (s, 1H), 6.60 (dd, J = 8.8, 2.4 Hz, 1H), 5.08 (dd, J = 12.9, 5.4 Hz, 1H), 4.08 (d, J = 12.9 Hz, 2H), 4.00 (s, 2H), 3.88 (s, 1H), 3.73 (s, 2H), 3.64 (s, 3H), 3.21 (s, 3H), 3.18−3.02 (m, 5H), 2.64−2.53 (m, 2H), 1.81−1.57 (m, 4H). ^{13}C NMR (100 MHz, DMSO) δ 173.29, 172.75, 170.58, 168.08, 167.44, 155.30, 134.52, 125.49, 118.10, 108.31, 49.21, 47.18, 45.12, 41.53, 39.56, 39.35, 37.26, 31.45, 27.93, 22.67, 22.53. LC-MS (ESI$^+$): calcd for $C_{39}H_{39}N_9O_7$ 745.30, found, 768.50 [M + Na]$^+$, 746.30 [M + H]$^+$. HPLC t_R = 12.736 min (95.78% purity).

4.1.5. N-(4-(4-(3-(2-(2-((2-(2,6-Dioxopiperidin-3-yl)-1,3-dioxoisoindolin-5-yl)oxy)ethoxy)ethoxy)propanoyl)piperazin-1-yl)-2-methoxyphenyl)-6-(1H-pyrazol-5-yl)picolinamide (LC-MI-4). White powder (52%). ^{1}H NMR (400 MHz, DMSO-d_6) δ 13.24 (s, 1H), 11.13 (s, 1H), 10.56 (s, 1H), 8.17 (s, 2H), 8.10 (t, J = 7.6 Hz, 1H), 8.06−8.00 (m, 1H), 7.90 (s, 1H), 7.81 (d, J = 8.3 Hz, 1H), 7.44 (d, J = 2.3 Hz, 1H), 7.35 (dd, J = 8.3, 2.3 Hz, 1H), 6.99 (d, J = 2.3 Hz, 1H), 6.75 (d, J = 2.6 Hz, 1H), 6.56 (dd, J = 8.9, 2.5 Hz, 1H), 5.12 (dd, J = 12.9, 5.4 Hz, 1H), 4.32−4.25 (m, 2H), 3.96 (s, 3H), 3.81−3.74 (m, 2H), 3.70−3.51 (m, 12H), 3.17 (t, J = 5.0 Hz, 2H), 3.12 (t, J = 5.2 Hz, 2H), 2.66−2.51 (m, 4H). ^{13}C NMR (100 MHz, DMSO) δ 173.26, 170.43, 169.34, 167.33, 167.26, 164.37, 134.36, 125.72, 123.50, 121.33, 109.33, 100.83, 70.41, 70.16, 69.10, 68.87, 67.32, 49.58, 49.41, 49.18, 45.32, 41.32, 40.58, 40.37, 40.17, 39.96, 39.75, 39.54, 39.33, 33.23, 31.41, 22.52. LC-MS (ESI$^+$): calcd for $C_{40}H_{42}N_8O_{10}$ 794.30, found, 817.49 [M + Na]$^+$, 795.43 [M + H]$^+$. HPLC t_R = 12.396 min (99.63% purity).

4.1.6. N-(4-(4-(3-(2-(2-(2-((2-(2,6-Dioxopiperidin-3-yl)-1,3-dioxoisoindolin-5-yl)oxy)ethoxy)ethoxy)propanoyl)piperazin-1-yl)-2-methoxyphenyl)-6-(1H-pyrazol-5-yl)picolinamide (LC-MI-5). White powder (49%). ^{1}H NMR (400 MHz, DMSO-d_6) δ 13.24 (s, 1H), 11.13 (s, 1H), 10.59 (s, 1H), 8.25 (s, 1H), 8.19 (s, 1H), 8.10 (t, J = 7.6 Hz, 1H), 8.06−8.00 (m, 1H), 7.93 (s, 1H), 7.81 (d, J = 8.3 Hz, 1H), 7.43 (d, J = 2.3 Hz, 1H), 7.35 (dd, J = 8.3, 2.3 Hz, 1H), 6.99 (s, 1H), 6.76 (s, 1H), 6.57 (dd, J = 8.9, 2.5 Hz, 1H), 5.12 (dd, J = 12.9, 5.4 Hz, 1H), 4.33−4.26 (m, 2H), 3.99 (s, 3H), 3.80−3.74 (m, 2H), 3.70−3.47 (m, 16H), 3.21−3.09 (m, 4H), 2.66−2.53 (m, 4H). ^{13}C NMR (100 MHz, DMSO) δ 173.24, 170.40, 169.36, 167.32, 167.25, 164.37, 134.34, 125.70, 123.49, 121.30, 109.32, 100.83, 70.42, 70.28, 70.23, 70.17, 69.11, 68.87, 67.31, 49.62, 49.43, 49.17, 45.34, 41.33, 40.59, 40.38, 40.17, 39.96, 39.75, 39.54, 39.33, 33.26, 31.42, 22.54. LC-MS (ESI$^+$): calcd for $C_{42}H_{46}N_8O_{11}$ 838.33, found, 861.48 [M + Na]$^+$, 839.55 [M + H]$^+$. HPLC t_R = 12.471 min (97.15% purity).

4.1.7. N-(4-(4-(6-((2-(2,6-Dioxopiperidin-3-yl)-1,3-dioxoisoindolin-4-yl)amino)hexanoyl)piperazin-1-yl)-2-methoxyphenyl)-6-(1H-pyrazol-5-yl)picolinamide (LC-MI-6). Yellow-green powder (57%). ^{1}H NMR (400 MHz, DMSO-d_6) δ 13.23 (s, 1H), 11.11 (s, 1H), 10.60 (s, 1H), 8.25 (s, 1H), 8.19 (s, 1H), 8.14−8.00 (m, 2H), 7.93 (s, 1H), 7.58 (dd, J = 8.6, 7.1 Hz, 1H), 7.10 (d, J = 8.6 Hz, 1H), 7.02 (d, J = 7.0 Hz, 1H), 6.99 (s, 1H), 6.76 (s, 1H), 6.61−6.50 (m, 2H), 5.06 (dd, J = 12.9, 5.4 Hz, 1H), 3.99 (s, 2H), 3.61 (q, J = 5.5 Hz, 4H), 3.36−3.26 (m, 2H), 3.14 (d, J = 15.4 Hz, 4H), 2.96−2.81 (m, 1H), 2.65−2.52 (m, 2H), 2.38 (t, J = 7.4 Hz, 2H), 1.59 (dp, J = 14.7, 7.2 Hz, 4H), 1.46−1.16 (m, 4H). ^{13}C NMR (100 MHz, DMSO) δ 173.29, 171.07, 170.58, 169.42, 167.78, 146.90, 136.75, 132.66, 117.65, 110.85, 109.47, 49.01, 45.23, 42.24, 41.34, 40.60, 40.40, 40.19, 39.98, 39.77, 39.56, 39.35, 32.61, 31.45, 29.03, 26.56, 25.00, 22.63. LC-MS (ESI$^+$): calcd for $C_{39}H_{41}N_9O_7$ 747.31, found, 770.30 [M + Na]$^+$, 748.37 [M + H]$^+$. HPLC t_R = 9.972 min (97.61% purity).

4.1.8. N-(4-(4-(8-((2-(2,6-Dioxopiperidin-3-yl)-1,3-dioxoisoindolin-4-yl)amino)octanoyl)piperazin-1-yl)-2-methoxyphenyl)-6-(1H-pyrazol-5-yl)picolinamide (LC-MI-7). Yellow-green powder (54%). ^{1}H NMR (400 MHz, DMSO-d_6) δ 13.24 (s, 1H), 11.11 (s, 1H), 10.60 (s, 1H), 8.26 (s, 1H), 8.18 (s, 1H), 8.10 (t, J = 7.6 Hz, 1H), 8.04 (d, J = 8.5 Hz, 1H), 7.93 (s, 1H), 7.58 (dd, J = 8.6, 7.0 Hz, 1H), 7.09 (d, J = 8.6 Hz, 1H), 7.01 (dd, J = 9.8, 3.6 Hz, 2H), 6.76 (s, 1H), 6.58 (dd, J = 8.8, 2.5 Hz, 1H), 6.52 (t, J = 6.0 Hz, 1H), 5.06 (dd, J = 12.9, 5.4 Hz, 1H), 3.98 (s, 3H), 3.60 (q, J = 5.8, 5.1 Hz, 4H), 3.29 (q, J = 6.7 Hz, 2H), 3.15 (d, J = 18.0 Hz, 3H), 2.65−2.52 (m, 2H), 2.35 (t, J = 7.4 Hz, 2H), 1.62−1.48 (m, 5H), 1.39−1.17 (m, 8H). ^{13}C NMR (100 MHz, DMSO) δ 173.29, 171.15, 170.57, 169.44, 167.78, 146.90, 136.74, 132.65, 117.64, 110.84, 109.47, 49.01, 45.24, 42.29, 41.32, 40.60, 40.39, 40.30, 40.18, 39.97, 39.76, 39.56, 39.35, 32.68, 31.45, 29.21, 29.12, 29.07, 26.72, 25.22, 22.63. LC-MS (ESI$^+$): calcd for $C_{41}H_{45}N_9O_7$ 775.34, found, 798.49 [M + Na]$^+$, 776.70 [M + H]$^+$. HPLC t_R = 9.961 min (97.20% purity).

4.1.9. N-(4-(4-(12-((2-(2,6-Dioxopiperidin-3-yl)-1,3-dioxoisoindolin-4-yl)amino)dodecanoyl)piperazin-1-yl)-2-methoxyphenyl)-6-(1H-pyrazol-5-yl)picolinamide (LC-MI-8). Yellow-green powder (48%). ^{1}H NMR (400 MHz, DMSO-d_6) δ 13.23 (s, 1H), 11.10 (s, 1H), 10.60 (s, 1H), 8.26 (d, J = 8.2 Hz, 1H), 8.19 (s, 1H), 8.09 (t, J = 7.5 Hz, 1H), 8.03 (d, J = 6.9 Hz, 1H), 7.93 (s, 1H), 7.57 (dd, J = 8.6,

https://doi.org/10.1021/acs.jmedchem.4c00181
J. Med. Chem. 2024, 67, 8060−8076

7.1 Hz, 1H), 7.07 (d, J = 8.6 Hz, 1H), 7.04−6.96 (m, 2H), 6.77 (s, 1H), 6.58 (dd, J = 8.9, 2.6 Hz, 1H), 6.50 (t, J = 5.9 Hz, 1H), 5.05 (dd, J = 12.9, 5.4 Hz, 1H), 3.98 (d, J = 6.3 Hz, 2H), 3.60 (q, J = 5.4, 5.0 Hz, 4H), 3.27 (q, J = 6.7 Hz, 2H), 3.15 (d, J = 17.8 Hz, 5H), 2.64−2.52 (m, 1H), 2.34 (t, J = 7.4 Hz, 2H), 1.53 (dt, J = 21.4, 7.4 Hz, 5H), 1.39−1.13 (m, 16H). ^{13}C NMR (100 MHz, DMSO) δ 173.28, 171.16, 170.56, 169.42, 167.77, 146.89, 136.72, 132.64, 110.82, 109.46, 49.01, 45.26, 42.30, 41.32, 40.61, 40.40, 40.19, 39.98, 39.77, 39.56, 39.36, 32.70, 31.45, 29.46, 29.42, 29.35, 29.24, 29.13, 26.78, 25.29, 22.63. LC-MS (ESI$^+$): calcd for $C_{45}H_{53}N_9O_7$ 831.41, found, 854.48 [M + Na]$^+$, 832.75 [M + H]$^+$. HPLC t_R = 12.360 min (99.02% purity).

4.1.10. N-(4-(4-(2-((2-(2,6-Dioxopiperidin-3-yl)-1,3-dioxoisoindolin-4-yl)amino)ethyl)amino)-2-oxoethyl)piperazin-1-yl)-2-methoxyphenyl)-6-(1H-pyrazol-5-yl)picolinamide (LC-MI-9). Yellow-green powder (46 mg, 52%). ^{1}H NMR (400 MHz, DMSO-d_6) δ 13.23 (s, 1H), 11.10 (s, 1H), 10.58 (s, 1H), 8.19 (s, 1H), 8.14−8.00 (m, 4H), 7.93 (s, 1H), 7.60 (dd, J = 8.6, 7.1 Hz, 1H), 7.23 (d, J = 8.6 Hz, 1H), 7.05 (d, J = 7.0 Hz, 1H), 6.99 (s, 1H), 6.76−6.69 (m, 2H), 6.53 (dd, J = 8.9, 2.5 Hz, 1H), 5.06 (dd, J = 12.9, 5.4 Hz, 1H), 3.97 (s, 3H), 3.51−3.40 (m, 2H), 3.18 (s, 4H), 2.99 (s, 2H), 2.65−2.51 (m, 6H), 1.38−1.17 (m, 4H). ^{13}C NMR (100 MHz, DMSO) δ 173.26, 170.55, 169.19, 167.78, 146.87, 136.71, 132.69, 117.75, 111.05, 109.69, 53.27, 49.01, 48.85, 41.86, 40.60, 40.39, 40.19, 39.98, 39.77, 39.56, 39.35, 38.19, 31.44, 29.47, 22.65. LC-MS (ESI$^+$): calcd for $C_{37}H_{38}N_{10}O_7$ 734.29, found, 757.30 [M + Na]$^+$, 735.44 [M + H]$^+$. HPLC t_R = 12.429 min (96.48% purity).

4.1.11. N-(4-(4-(2-((5-((2-(2,6-Dioxopiperidin-3-yl)-1,3-dioxoisoindolin-4-yl)amino)pentyl)amino)-2-oxoethyl)piperazin-1-yl)-2-methoxyphenyl)-6-(1H-pyrazol-5-yl)picolinamide (LC-MI-10). Yellow-green powder (52%). ^{1}H NMR (400 MHz, DMSO-d_6) δ 13.23 (s, 1H), 11.10 (s, 1H), 10.59 (s, 1H), 8.20 (d, J = 15.0 Hz, 2H), 8.10 (t, J = 7.6 Hz, 1H), 8.09−8.00 (m, 1H), 7.93 (s, 1H), 7.78 (t, J = 5.7 Hz, 1H), 7.63−7.54 (m, 1H), 7.10 (d, J = 8.6 Hz, 1H), 7.02 (d, J = 7.0 Hz, 1H), 6.99 (s, 1H), 6.73 (s, 1H), 6.54 (dt, J = 11.8, 4.4 Hz, 2H), 5.05 (dd, J = 12.9, 5.4 Hz, 1H), 3.98 (s, 3H), 3.30 (dd, J = 13.4, 6.9 Hz, 3H), 3.20 (d, J = 5.7 Hz, 5H), 3.13 (q, J = 6.6 Hz, 2H), 2.98 (s, 2H), 2.95−2.81 (m, 2H), 2.63−2.51 (m, 4H), 1.66−1.28 (m, 6H). ^{13}C NMR (100 MHz, DMSO) δ 173.28, 170.56, 169.43, 169.34, 167.77, 146.89, 136.76, 132.65, 117.67, 110.87, 109.49, 53.29, 49.01, 48.89, 42.26, 40.60, 40.39, 40.19, 39.98, 39.77, 39.56, 39.35, 38.53, 31.44, 29.40, 28.82, 24.15, 22.63. LC-MS (ESI$^+$): calcd for $C_{40}H_{44}N_{10}O_7$ 776.34, found, 799.49 [M + Na]$^+$, 777.43 [M + H]$^+$. HPLC t_R = 12.414 min (96.90% purity).

4.1.12. N-(4-(4-(2-((8-((2-(2,6-Dioxopiperidin-3-yl)-1,3-dioxoisoindolin-4-yl)amino)octyl)amino)-2-oxoethyl)piperazin-1-yl)-2-methoxyphenyl)-6-(1H-pyrazol-5-yl)picolinamide (LC-MI-11). Yellow-green powder (49%). ^{1}H NMR (400 MHz, DMSO-d_6) δ 13.24 (s, 1H), 11.10 (s, 1H), 10.59 (s, 1H), 8.22 (dd, J = 16.6, 8.2 Hz, 2H), 8.10 (t, J = 7.6 Hz, 1H), 8.04 (d, J = 7.6 Hz, 1H), 7.94 (s, 1H), 7.75 (t, J = 6.0 Hz, 1H), 7.61−7.53 (m, 1H), 7.07 (d, J = 8.6 Hz, 1H), 7.04−6.96 (m, 2H), 6.73 (s, 1H), 6.59−6.47 (m, 2H), 5.06 (dd, J = 12.9, 5.4 Hz, 1H), 3.98 (s, 3H), 3.31−3.18 (m, 6H), 3.10 (q, J = 6.7 Hz, 2H), 2.98 (s, 2H), 2.64−2.55 (m, 6H), 1.61−1.18 (m, 14H). ^{13}C NMR (100 MHz, DMSO) δ 173.29, 170.57, 169.43, 169.29, 167.77, 146.88, 136.73, 132.63, 117.59, 110.84, 109.46, 61.74, 53.28, 49.01, 48.91, 42.30, 40.59, 40.38, 40.17, 39.96, 39.75, 39.55, 39.34, 38.65, 31.44, 29.65, 29.20, 29.14, 26.81, 26.75, 22.63. LC-MS (ESI$^+$): calcd for $C_{43}H_{50}N_{10}O_7$ 818.39, found, 841.48 [M + Na]$^+$, 819.62 [M + H]$^+$. HPLC t_R = 11.866 min (96.18% purity).

N-(4-(4-(2-((2-(2-((2-(2,6-dioxopiperidin-3-yl)-1,3-dioxoisoindolin-4-yl)amino)ethoxy)ethyl)amino)-2-oxoethyl)piperazin-1-yl)-2-methoxyphenyl)-6-(1H-pyrazol-5-yl)picolinamide (LC-MI-12). Yellow powder (49%). ^{1}H NMR (400 MHz, DMSO-d_6) δ 13.23 (s, 1H), 11.11 (s, 1H), 10.58 (s, 1H), 8.22 (d, J = 11.2 Hz, 2H), 8.10 (t, J = 7.6 Hz, 1H), 8.04 (d, J = 8.5 Hz, 1H), 7.93 (s, 1H), 7.79 (s, 1H), 7.58 (t, 1H), 7.14 (d, J = 8.6 Hz, 1H), 7.04 (d, J = 7.0 Hz, 1H), 6.99 (s, 1H), 6.70 (s, 1H), 6.61 (t, J = 5.7 Hz, 1H), 6.51 (dd, J = 8.9, 2.5 Hz, 1H), 5.06 (dd, J = 12.9, 5.4 Hz, 1H), 4.00−3.93 (m, 3H), 3.64 (t, J = 5.4 Hz, 2H), 3.50 (dt, J = 13.9, 5.7 Hz, 4H), 3.32 (q, J = 6.0 Hz, 3H), 3.18 (s, 5H), 3.00 (s, 2H), 2.64−2.52 (m, 6H). ^{13}C NMR (100 MHz, DMSO) δ 173.27, 170.53, 169.45, 167.74, 146.86, 136.73, 132.53, 117.89, 111.21, 109.73, 69.33, 69.05, 53.21, 49.03, 48.89, 42.23, 40.59, 40.39, 40.18, 39.97, 39.76, 39.55, 39.34, 38.52, 31.44, 22.62. LC-MS (ESI$^+$): calcd for $C_{39}H_{42}N_{10}O_8$ 778.32, found, 779.56 [M + H]$^+$. HPLC t_R = 10.035 min (96.83% purity).

4.1.13. N-(4-(4-(2-((2-(2-((2-(2,6-Dioxopiperidin-3-yl)-1,3-dioxoisoindolin-4-yl)amino)ethoxy)ethoxy)ethyl)amino)-2-oxoethyl)-piperazin-1-yl)-2-methoxyphenyl)-6-(1H-pyrazol-5-yl)picolinamide (LC-MI-13). Yellow powder (49%). ^{1}H NMR (400 MHz, DMSO-d_6) δ 13.23 (s, 1H), 11.10 (s, 1H), 10.58 (s, 1H), 8.20 (d, J = 9.3 Hz, 2H), 8.10 (t, J = 7.5 Hz, 1H), 8.04 (d, J = 6.9 Hz, 1H), 7.94 (s, 1H), 7.75 (t, J = 5.9 Hz, 1H), 7.56 (dd, J = 8.6, 7.1 Hz, 1H), 7.10 (d, J = 8.6 Hz, 1H), 7.02 (d, J = 7.0 Hz, 1H), 6.99 (s, 1H), 6.71 (s, 1H), 6.60 (t, J = 5.8 Hz, 1H), 6.53 (dd, J = 8.9, 2.5 Hz, 1H), 5.06 (dd, J = 12.9, 5.4 Hz, 1H), 3.92 (d, J = 43.5 Hz, 3H), 3.66−3.51 (m, 6H), 3.45 (p, J = 5.7 Hz, 5H), 3.37−3.24 (m, 3H), 3.19 (t, J = 4.8 Hz, 4H), 2.99 (s, 2H), 2.64−2.52 (m, 6H). ^{13}C NMR (100 MHz, DMSO) δ 173.27, 170.55, 169.57, 169.42, 167.74, 146.81, 136.66, 132.53, 117.83, 111.15, 109.71, 70.28, 70.01, 69.53, 69.34, 53.23, 49.03, 48.96, 42.14, 40.60, 40.39, 40.18, 39.97, 39.76, 39.55, 39.35, 38.58, 31.45, 22.61. LC-MS (ESI$^+$): calcd for $C_{41}H_{46}N_{10}O_9$ 822.34, found, 823.62 [M + H]$^+$. HPLC t_R = 10.205 min (95.49% purity).

4.1.14. N-(4-(4-(17-((2-(2,6-Dioxopiperidin-3-yl)-1,3-dioxoisoindolin-4-yl)amino)-2-oxo-6,9,12,15-tetraoxa-3-azaheptadecyl)-piperazin-1-yl)-2-methoxyphenyl)-6-(1H-pyrazol-5-yl)picolinamide (LC-MI-14). Yellow powder (42%). ^{1}H NMR (400 MHz, DMSO-d_6) δ 13.23 (s, 1H), 11.10 (s, 1H), 10.59 (s, 1H), 8.26−8.16 (m, 1H), 8.13−8.00 (m, 2H), 7.93 (s, 1H), 7.76 (t, J = 5.8 Hz, 1H), 7.58 (ddd, J = 13.9, 8.6, 7.1 Hz, 1H), 7.18−6.96 (m, 3H), 6.73 (s, 1H), 6.58 (tt, J = 9.0, 4.6 Hz, 3H), 5.06 (dt, J = 13.0, 4.9 Hz, 1H), 4.03−3.92 (m, 2H), 3.67−3.38 (m, 17H), 3.33−3.16 (m, 6H), 3.00 (s, 2H), 2.95−2.82 (m, 5H), 2.59 (dt, J = 17.9, 6.9 Hz, 5H). ^{13}C NMR (100 MHz, DMSO) δ 173.27, 170.53, 169.57, 169.39, 167.75, 146.84, 136.65, 132.53, 117.85, 111.12, 109.69, 70.34, 70.30, 70.26, 70.22, 70.16, 70.00, 69.44, 69.32, 69.23, 53.24, 49.02, 42.14, 40.59, 40.38, 40.17, 39.97, 39.76, 39.55, 39.34, 38.56, 31.45, 22.62. LC-MS (ESI$^+$): calcd for $C_{45}H_{54}N_{10}O_{11}$ 910.40, found, 911.33 [M + H]$^+$. HPLC t_R = 12.429 min (99.10% purity).

4.1.15. N-(4-(4-(1-(1-(2-(2,6-Dioxopiperidin-3-yl)-1,3-dioxoisoindolin-5-yl)piperidin-4-yl)-1,12-dioxo-5,8-dioxa-2,11-diazatridecan-13-yl)piperazin-1-yl)-2-methoxyphenyl)-6-(1H-pyrazol-5-yl)-picolinamide (LC-MI-15). Yellow powder (62%). ^{1}H NMR (400 MHz, DMSO-d_6) δ 13.22 (s, 1H), 11.07 (s, 1H), 10.58 (s, 1H), 8.23 (s, 1H), 8.18 (s, 1H), 8.09 (t, J = 7.6 Hz, 1H), 8.02 (d, J = 8.3 Hz, 1H), 7.93 (s, 1H), 7.87 (t, J = 5.6 Hz, 1H), 7.77 (s, 1H), 7.63 (d, J = 8.5 Hz, 1H), 7.30 (d, J = 2.3 Hz, 1H), 7.20 (dd, J = 8.6, 2.4 Hz, 1H), 6.98 (s, 1H), 6.73 (s, 1H), 6.56 (dd, J = 8.9, 2.5 Hz, 1H), 5.06 (dd, J = 12.9, 5.4 Hz, 1H), 4.07−3.95 (m, 5H), 3.56−3.37 (m, 9H), 3.31−3.14 (m, 9H), 3.06−2.81 (m, 6H), 2.61 (s, 5H), 1.74 (d, J = 13.0 Hz, 2H), 1.59 (q, J = 10.3, 9.8 Hz, 2H). ^{13}C NMR (100 MHz, DMSO) δ 174.44, 173.28, 170.57, 168.05, 167.41, 155.30, 134.47, 125.42, 118.14, 118.09, 108.32, 70.07, 69.95, 69.53, 69.44, 53.24, 49.20, 47.32, 41.88, 40.60, 40.40, 40.19, 39.98, 39.77, 39.56, 39.35, 38.91, 38.58, 31.44, 28.01, 22.65. LC-MS (ESI$^+$): calcd for $C_{47}H_{55}N_{11}O_{10}$ 933.41, found, 956.59 [M + Na]$^+$, 934.59 [M + H]$^+$. HPLC t_R = 9.552 min (95.80% purity).

4.2. Cell Culture. The mouse macrophage cell line, RAW264.7, was kindly provided by the Cell Bank (Chinese Academy of Sciences).. Human peripheral blood mononuclear cells (PBMCs) were purchased from AllCell Biosciences. RAW264.7 cells were cultured in the Dulbecco's modified Eagle's medium (DMEM; Cat. No. BC-M-005; Bio-Channel) containing 10% fetal bovine serum (FBS; Cat. No. BC-SE-FBS07; Bio-Channel) and 1% penicillin/streptomycin (Cat. No. BL505A; Biosharp) at 37 °C with 5% CO_2. RAW264.7-NF-κB-RE-EGFP cells were cultured in DMEM containing 10% FBS, 1% penicillin/streptomycin, and 200 μg/mL Geneticin (Cat. No. 11811031; ThermoFisher) at 37 °C with 5% CO_2. Human PBMCs were cultured in the Roswell Park Memorial Institute-1640 medium (Cat. No. BC-M-017; BioChannel) containing 10% FBS (Cat. No. BC-SE-FBS07; Bio-Channel) and 1% penicillin/streptomycin (Cat. No. BL505A; Biosharp) at 37 °C with 5% CO_2.

https://doi.org/10.1021/acs.jmedchem.4c00181
J. Med. Chem. 2024, 67, 8060−8076

4.3. Western Blotting Assay. Proteins were isolated from the cell lysate and centrifuged at 12000 rpm for 10 min at 4 °C. After removing the supernatant, protein concentration was detected using the BCA method and normalized to the same protein concentration. Proteins were denatured at 100 °C for 10 min after diluting the protein with a 5× protein buffer. Samples were separated by SDS-PAGE and transferred to membranes. A chemiluminescence reagent (NcmECL Ultra; Cat. No. P10300A; NCM Biotech) was used to visualize the antibodies with the Vilber Fusion FX system.

The following primary antibodies were used: anti-β-tubulin (1:5000; Cat. No. ET1602−4), anti-β-actin (1:5000; Cat. No. R1207−1), anti-IκB-α (1:1000; Cat. No. ET1603−6), anti-NF-κB p65 (1:1000; Cat. No. ET1603−12), anti-p38 (1:1000; Cat. No. ET1702−65), anti-p-JNK1/2/3(Tyr183/Tyr183/Tyr221) (1:1000; Cat. No. ET1609−42), anti-JNK1/2/3 (1:2000; Cat. No. ET1601−28); anti-SALL4 (1:1000; Cat. No. HA601145); anti-IKZF1 (1:1000; Cat. No. ET7107−25); anti-IKZF3 (1:1000; Cat. No. HA720110) were purchased from HUABIO. Anti-p-p38(Thr180/Tyr182) (1:1000, Cat. No. #AF4001; Affinity Biosciences) and anti-p-NF-κB p65(Ser468) (1:2000; Cat. No. 82335−1-RR; Proteintech) antibodies were also used here. Additionally, the anti-p-ERK1/2(Thr202/Tyr204) (1:2000; Cat. No. #4370), anti-ERK1/2 (1:2000; Cat. No. #4695), anti-MyD88 (1:1000; Cat. No. #4283), and anti-IRAK4 (1:1000; Cat. No. #4363) antibodies were all purchased from Cell Signaling Technology.

4.4. RNA Extraction and Quantitative Polymerase Chain Reaction (qPCR). Next, mRNA from RAW264.7 cells and mouse lung tissues was analyzed via standard qPCR. AG RNAex Pro RNA Extraction Reagent (Cat. No. AG21101; Accurate Biotechnology) and SteadyPure Universal RNA Extraction Kit (Cat. No. AG21024; Accurate Biotechnology) was used to isolate the total RNA, and RNA concentration was determined using the NanoDrop 2000 spectrophotometer (Thermo Fisher Scientific), following the manufacturers' instructions. Then, cDNA was synthesized using the Evo M-MLV Mix Kit with gDNA Clean for qPCR (Cat. No. AG11728; Accurate Biotechnology), according to the manufacturer's protocol. Gene expression levels were measured via relative quantification using the SYBR Green Premix Pro Taq HS qPCR Kit (Cat. No. AG11733; Accurate Biotechnology). qPCR amplifications were performed using the CFX Connect Real-Time system (Bio-Rad). The $2^{-\Delta\Delta Ct}$ method was used to analyze the relative expression levels.

The following primer sequences were used here:

Mouse *TNF-α* forward: Forward primer (5′−3′), TGATCCGCGACGTGGAA; reverse primer (5′−3′), ACCGCCTGGAGTTCTGGAA.

Mouse *IL-6* forward: Forward primer (5′−3′), GAGGATACCACTCCCAACAGACC; reverse primer (5′−3′), AAGTGCATCATCGTTGTTCATACA.

Mouse *GAPDH* forward: Forward primer (5′−3′), GGAGCGAGATCCCTCCAAAAT; reverse primer (5′−3′), GGCTGTTGTCATACTTCTCATGG.

4.5. Detection of TNF-α and IL-6 Secretion. TNF-α (Cat. No. 88−7324; ThermoFisher) and IL-6 (Cat. No. 88−7064; Thermo Fisher Scientific) levels in the collected culture medium and BALF of each mice group were determined via ELISA, following the manufacturer's instructions.

4.6. Immunofluorescence Analysis. To assess NF-κB activation, cells were stained for NF-κB p65 translocation. RAW264.7 cells were fixed by 2% formaldehyde for 2 min, permeabilized with 0.5% Triton X-100 in PBS, and blocked with BSA for 1 h. Fixed cells were incubated with the anti-NF-κB p65 antibody (1:100) overnight. After washing thrice with PBS, the cells were stained with Alexa Fluor 647-conjugated secondary antibodies (1:500; Cat. No. A0468; Beyotime Biotechnology) for 1 h and DAPI. Microscopy was performed using the EVOS M7000 cell imaging system (Thermo Fisher Scientific). To evaluate IRAK4 degradation, cells were stained for IRAK4. Human PBMCs were fixed with 2% formaldehyde. Fixed cells were incubated with anti-IRAK4 antibody (1:100; Cat. No. ab119942; Abcam) and treated as NF-κB.

4.7. Flow Cytometry. EGFP fluorescence intensity of RAW264.7-NF-κB-RE-EGFP cells was measured to determine NF-κB activation. Briefly, RAW264.7-NF-κB-RE-EGFP cells (10^6 cells/well) were seeded in a 6-well plate, treated with the compound or DMSO for 1 h, and stimulated with 0.5 μg/mL LPS for 6 h. Then, the cells were suspended in the eBioscience Flow Cytometry Staining Buffer (Cat. No. 00−4222−57; ThermoFisher).

TLR4 endocytosis was quantified via flow cytometry as previously described.[38] Briefly, RAW264.7 cells (10^6 cells/well) were pretreated with LC-MI-3, JH-I-25, or vehicle for 6 h and stimulated with 0.5 μg/mL LPS for 30 min (37 °C, 5% CO_2). After incubation, 2 mL of ice-cold eBioscience Flow Cytometry Staining Buffer was added, and the cells were centrifuged and washed twice with the eBioscience Flow Cytometry Staining Buffer. The cells were then resuspended in 100 μL of eBioscience Flow Cytometry Staining Buffer containing PE-conjugated anti-TLR4 (4 μg/mL; Cat. No. 145403; BioLegend) or 100 μL of eBioscience Flow Cytometry Staining Buffer containing PE-conjugated IgG2a κ-chain isotype-matched control (4 μg/mL; Cat. No. 400507; BioLegend) and incubated on ice for 30 min in the dark. After three washes, the samples were resuspended in the eBioscience Flow Cytometry Staining Buffer.

Both EGFP and PE fluorescence were measured using the BD Accuri C6 Plus flow cytometer (BD Biosciences) and analyzed using the FlowJo software (BD Biosciences). The percentage of surface TLR4 was calculated as follows: $(MFI_{test} - MFI_{isotype\ control})/(MFI_{control} - MFI_{isotype\ control})$.

4.8. Kinase Selectivity Profile. The kinase selectivity evaluation of LC-MI-3 was studied on Eurofins KINOMEscan platform. LC-MI-3 was tested at the concentration of 1 μM against 468 targets (scanMax, eurofinsdiscoveryservices.com).

4.9. *E. coli* Infection Assay. Next, bacterial infections were induced. *E. coli* strain BL21 was grown in the LB Broth (Cat. No. A507002; Sangon Biotech), and the density was determined at 600 nm (OD600) using the NanoDrop2000 spectrophotometer. The corresponding colony-forming units (CFU) were determined on the LB agar. RAW264.7 cells were seeded in a 6-well plate overnight and pretreated with LC-MI-3, JH-I-25, or vehicle for 6 h. Then, the medium containing 10^{10} CFU/mL *E. coli* was added to the plate, centrifuged to facilitate contact between bacteria and cells, and incubated for 6 h. Cells and medium were collected for qPCR and ELISA.

4.10. Animals. C57BL/6 mice (20 ± 2 g) were obtained from the Hangzhou Medical College Experimental Animal Center (Hangzhou, China). All animals were housed under controlled room temperature (22 ± 1 °C), with a 12:12 h light-dark cycle and fed a standard rodent diet and water. All animals received humane care according to the institutional animal care guidelines approved by the Experimental Animal Ethics Committee of Hangzhou Medical College.

4.11. Pharmacokinetic (PK) Study. LC-MI-3 was dissolved in a vehicle containing 10% DMSO, 10% Solutol, and 80% (20% HP-β-CD in saline). The pH was adjusted to 9.5. Male SD rats were administered 3 mg/kg LC-MI-3 solution intravenously (i.v.) and 20 mg/kg p.o.. Blood samples of rats were collected. Plasma supernatant samples were analyzed via LC−MS/MS (TQ6500+).

4.12. Metabolite Profiling of LC-MI-3 in Rat Hepatocytes. Rat hepatocytes are incubated LC-MI-3 (10 μM) for 0, 1, or 2 h at 37 °C. Then the mixture incubated with acetonitrile (0.1% formic acid) followed by centrifugation for 5 min. The supernatant was collected and evaporated using SpeedVac (Savant SPD1030, Thermo Scientific, USA). Dried samples were reconstituted in acetonitrile:water (40:60; v:v, 0.1% formic acid), and centrifuged. Supernatant was then analyzed by LC-MS/MS. Each sample was analyzed on a Waters ACQUITY UPLC system (Waters) equipped with an CORTECS C18+ column (Waters CORTECS C18+, 2.1 × 50 mm, 1.6 μm). Mass spectrometric data were obtained by Waters xevo G3 Q-TOF Mass Spectrometer equipped with a Dual Agilent Jet Stream electrospray ionization (ESI) source. The ESI source was set in positive/negative ionization mode.

4.13. TMT-Labeled Quantitative Proteomics Assay. To obtain TMT-labeled quantitative proteomics data, RAW 264.7 cells

https://doi.org/10.1021/acs.jmedchem.4c00181
J. Med. Chem. 2024, 67, 8060−8076

were first transplanted into 10 cm Petri dishes. Then, 500 nM LC-MI-3 and blank control DMSO were added to the culture medium, respectively, and treated for 6 h. For each group, three biological replicates were set. Then, the medium was removed and cells were collected by centrifuge at 4 °C, 700g. Proteomics sequencing services, containing protein extraction, protease digestion, TMT/iTRAQ labeling, HPLC separation, liquid-phase tandem mass spectrometry, database search, and bioinformatics analysis, were provided by Lianchuan Biotechnology (Hangzhou, China). The scatter diagram was plotted using GraphPad Prism 8.

4.14. In Vivo LPS-induced ALI Model. Mice were randomly divided into four groups (n = 8): control (Con), LPS-induced ALI (LPS; 5 mg/kg), LPS-induced ALI mice treated with 20 mg/kg LC-MI-3 (LPS + LC-MI-3), and LPS-induced ALI mice treated with 20 mg/kg JH-I-25 (LPS + JH-I-25) groups. Mice were treated with LC-MI-3 and JH-I-25 via intragastric administration at 200 μL/20 g body weight; the control and LPS groups received the same volume of vehicle (5% DMSO, 30% PEG-400, and 65% saline). After treatment with the vehicle, LC-MI-3, or JH-I-25 for 12 and 1 h, the mice were challenged with 5 mg/kg LPS via intratracheal instillation. Six hours after sacrificing the mice, samples, including BALF and lung tissue samples, were collected. The collected BALF was centrifuged at 1000 rpm for 10 min at 4 °C, and the supernatant was used for cytokine (TNF-α and IL-6) concentration determination.

4.15. In Vivo *E. coli*-Induced Sepsis Model. Viable *E. coli* in 0.2 mL PBS (2×10^9 CFU/mouse) was injected into the peritoneal cavity of 8-week-old male C57BL/6 mice. To test the pharmacological effects of IRAK4 inhibitors in these models, 8-week-old male C57BL/6 mice were pretreated with 20 mg/kg JH-I-25, LC-MI-3, or vehicle (5% DMSO, 30% PEG-400, and 65% saline) via intragastric injection twice a day for 3 days before *E. coli* injection. After injection, the compound or vehicle treatment was continued twice a day until the mice died or the experiment ended on the sixth day. The survival of mice was monitored during the experimental period. If they showed signs of death or at the end of the experiment, the mice were sacrificed, and their spleens were collected for immunohistochemical analysis.

4.16. In Vivo IMQ-Induced Psoriasis Model. Male C57BL/6 mice were randomized into different groups by body weight and dosed via oral gavage with 20 mg/kg JH-I-25 or LC-MI-3 twice daily or dexamethasone (as an experimental reference compound) at 3 mg/kg twice daily. Control animals were dosed with vehicle (5% DMSO, 30% PEG-400, and 65% saline). Psoriasis was induced via daily application of 3.125 mg/mouse IMQ cream (United Laboratories) on the shaved back region of the mice for 6 days. Disease severity was monitored daily by recording the skin thickness, erythema, and scaling. Skin thickness was measured using a micrometer. On day 6, the mice were sacrificed, and their back skin was collected for immunohistochemical analysis. Erythema and scaling were scored on a scale of 0−4 (0 = no erythema/scaling, 1 = slight redness/scaling, 2 = moderate redness/scaling, 3 = marked redness/scaling, and 4 = severe redness/scaling).

4.17. Immunohistochemical Determination. Next, lung tissues were immobilized in 4% paraformaldehyde for 48 h, dehydrated with graded alcohol, and embedded in paraffin. Paraffin-embedded sections (5 μm) were processed for immunohistochemical (hematoxylin and eosin) staining, evaluated via light microscopy, and quantitatively analyzed using the ImageJ software.

Paraffin-embedded sections were deparaffinized and rehydrated, and antigens were recovered by boiling in citrate buffer (pH 6.0) for 10 min. Endogenous peroxidase was blocked using 3% hydrogen peroxide. Then, the sections were incubated with 5% BSA for 1 h, followed by incubation with F4/80 (1:200, Cat. No. #70076, Cell Signaling Technology) or Ki67 (1:500, Cat. No. #9179, Cell Signaling Technology) primary antibody for 12 h on a shaker at 4 °C. The sections were then incubated with an HRP-conjugated secondary antibody for 15 min, developed with DAB chromogen, counterstained with hematoxylin, and observed under an inverted fluorescent microscope. The histochemical staining intensity was determined using the ImageJ software.

4.18. Statistical Analysis. All data were obtained from at least three independent replicates and represented as the mean ± standard error of the mean. Statistical analyses were performed using the GraphPad Prism 8.0 software (GraphPad, San Diego, CA, USA). Comparisons between two groups and among multiple groups were performed using a two-tailed unpaired Student's *t*-test and one-way analysis of variance followed by Dunnett's posthoc test, respectively. Statistical significance was set at $P < 0.05$. Post-tests were run only if $P < 0.05$, with no significant variance in homogeneity.

■ ASSOCIATED CONTENT

Supporting Information

The Supporting Information is available free of charge at https://pubs.acs.org/doi/10.1021/acs.jmedchem.4c00181.

Supplemental Figures S1−S8, Supplemental Tables S1 and S2, NMR, MS, and HPLC data (PDF)

Molecular formula strings. (CSV)

■ AUTHOR INFORMATION

Corresponding Authors

Lingfeng Chen − *School of Pharmacy, Hangzhou Medical College, Hangzhou 310014 Zhejiang, China;* orcid.org/0000-0003-0089-6559; Phone: +86-571-88215622; Email: lfchen@hmc.edu.cn

Guang Liang − *School of Pharmacy, Hangzhou Medical College, Hangzhou 310014 Zhejiang, China;* orcid.org/0000-0002-8278-849X; Email: wzmcliangguang@163.com

Authors

Ruixiang Luo − *School of Pharmacy, Hangzhou Medical College, Hangzhou 310014 Zhejiang, China*

Lin Ma − *School of Pharmacy, Hangzhou Medical College, Hangzhou 310014 Zhejiang, China*

Ying Xu − *School of Pharmacy, Hangzhou Medical College, Hangzhou 310014 Zhejiang, China*

Jiaqi Cao − *School of Pharmacy, Hangzhou Medical College, Hangzhou 310014 Zhejiang, China*

Zheng Jiang − *School of Pharmacy, Hangzhou Medical College, Hangzhou 310014 Zhejiang, China*

Shiyan Chen − *School of Pharmacy, Hangzhou Medical College, Hangzhou 310014 Zhejiang, China*

Xiaohao Huang − *School of Pharmacy, Hangzhou Medical College, Hangzhou 310014 Zhejiang, China*

Mingwan Zhang − *Department of Pharmacy, Tongde Hospital of Zhejiang Province, Hangzhou 310000 Zhejiang, China*

Lei Zheng − *School of Pharmacy, Hangzhou Medical College, Hangzhou 310014 Zhejiang, China*

Yawen Zhang − *School of Pharmacy, Hangzhou Medical College, Hangzhou 310014 Zhejiang, China;* orcid.org/0000-0001-7229-5969

Lina Yin − *School of Pharmacy, Hangzhou Medical College, Hangzhou 310014 Zhejiang, China*

Jie Yu − *School of Pharmacy, Hangzhou Medical College, Hangzhou 310014 Zhejiang, China*

Xiaochun Zheng − *School of Pharmacy and Center for Clinical Pharmacy, Cancer Center, Department of Pharmacy, Zhejiang Provincial People's Hospital(Affiliated People's Hospital), Hangzhou Medical College, Hangzhou 310014 Zhejiang, China*

Lulu Zheng − *Department of Pharmacy, Tongde Hospital of Zhejiang Province, Hangzhou 310000 Zhejiang, China*

Ping Huang − *School of Pharmacy and Center for Clinical Pharmacy, Cancer Center, Department of Pharmacy,*

https://doi.org/10.1021/acs.jmedchem.4c00181
J. Med. Chem. 2024, 67, 8060−8076

Zhejiang Provincial People's Hospital(Affiliated People's Hospital), Hangzhou Medical College, Hangzhou 310014 Zhejiang, China

Complete contact information is available at: https://pubs.acs.org/10.1021/acs.jmedchem.4c00181

Author Contributions

#L.C., R.L., L.M., and Y.X. contributed equally to this work. L.C., G.L., and L.M. conceived and proposed this project. L.M. and L.Z. synthesized the target compounds. R.L., J.C., J.Z., S.C., X.H., M.Z., and Y.X. completed drug screening and cell-based studies. Y.Z. and R. L. participated in the in vivo studies. X.Z., L.Z., and P.H. contributed to the reviewing of the manuscript. L.C. wrote the manuscript with input from all authors.

Funding

This work was supported by the National Natural Science Foundation of China (82103999 to L.C.), Natural Science Funding of Zhejiang Province (LQ22H300007 and LR24H300001 to L.C., LQ21H31006 to J.Y., LYQ20H300002 to M.Z.), Zhejiang Medical and Health Science Project (2023KY622 to L.Z.), Zhejiang Provincial Key Scientific Project (2021C03041 to G.L.), Huadong Medicine Joint Funds of Zhejiang Provincial Natural Science Foundation of China (LHDMY23H310004 to L.Z.), and Shanghai Frontiers Science Center of Drug Target Identification and Delivery (ZXWH2170101/019 to L.C.).

Notes

The authors declare no competing financial interest.

REFERENCES

(1) Chen, L.; Zheng, L.; Chen, P.; Liang, G. Myeloid Differentiation Primary Response Protein 88 (MyD88): The Central Hub of TLR/IL-1R Signaling. *J. Med. Chem.* **2020**, *63* (22), 13316−13329.

(2) Gay, N. J.; Symmons, M. F.; Gangloff, M.; Bryant, C. E. Assembly and localization of Toll-like receptor signalling complexes. *Nat. Rev. Immunol* **2014**, *14* (8), 546−558.

(3) Chaudhary, D.; Robinson, S.; Romero, D. L. Recent advances in the discovery of small molecule inhibitors of interleukin-1 receptor-associated kinase 4 (IRAK4) as a therapeutic target for inflammation and oncology disorders. *J. Med. Chem.* **2015**, *58* (1), 96−110.

(4) Li, X. IRAK4 in TLR/IL-1R signaling: possible clinical applications. *Eur. J. Immunol.* **2008**, *38* (3), 614−618.

(5) Lavazais, S.; Jargosch, M.; Dupont, S.; Labeguere, F.; Menet, C.; Jagerschmidt, C.; Ohm, F.; Kupcsik, L.; Parent, I.; Cottereaux, C.; et al. IRAK4 inhibition dampens pathogenic processes driving inflammatory skin diseases. *Sci. Transl Med.* **2023**, *15* (683), No. eabj3289.

(6) Lin, S. C.; Lo, Y. C.; Wu, H. Helical assembly in the MyD88-IRAK4-IRAK2 complex in TLR/IL-1R signalling. *Nature* **2010**, *465* (7300), 885−890.

(7) Ferrao, R.; Zhou, H.; Shan, Y.; Liu, Q.; Li, Q.; Shaw, D. E.; Li, X.; Wu, H. IRAK4 dimerization and trans-autophosphorylation are induced by Myddosome assembly. *Mol. Cell* **2014**, *55* (6), 891−903.

(8) Danto, S. I.; Shojaee, N.; Singh, R. S. P.; Li, C.; Gilbert, S. A.; Manukyan, Z.; Kilty, I. Safety, tolerability, pharmacokinetics, and pharmacodynamics of PF-06650833, a selective interleukin-1 receptor-associated kinase 4 (IRAK4) inhibitor, in single and multiple ascending dose randomized phase 1 studies in healthy subjects. *Arthritis Res. Ther* **2019**, *21* (1), 269.

(9) Li, Q.; Li, R.; Yin, H.; Wang, S.; Liu, B.; Li, J.; Zhou, M.; Yan, Q.; Lu, L. Oral IRAK4 inhibitor BAY-1834845 prevents acute respiratory distress syndrome. *Biomed Pharmacother* **2022**, *153*, No. 113459.

(10) Bothe, U.; Gunther, J.; Nubbemeyer, R.; Siebeneicher, H.; Ring, S.; Bomer, U.; Peters, M.; Rausch, A.; Denner, K.; Himmel, H.; et al. Discovery of IRAK4 Inhibitors BAY1834845 (Zabedosertib) and BAY1830839. *J. Med. Chem.* **2024**, *67* (2), 1225−1242.

(11) Bai, Y. R.; Yang, W. G.; Hou, X. H.; Shen, D. D.; Zhang, S. N.; Li, Y.; Qiao, Y. Y.; Wang, S. Q.; Yuan, S.; Liu, H. M. The recent advance of Interleukin-1 receptor associated kinase 4 inhibitors for the treatment of inflammation and related diseases. *Eur. J. Med. Chem.* **2023**, *258*, No. 115606.

(12) Gummadi, V. R.; Boruah, A.; Ainan, B. R.; Vare, B. R.; Manda, S.; Gondle, H. P.; Kumar, S. N.; Mukherjee, S.; Gore, S. T.; Krishnamurthy, N. R.; et al. Discovery of CA-4948, an Orally Bioavailable IRAK4 Inhibitor for Treatment of Hematologic Malignancies. *ACS Med. Chem. Lett.* **2020**, *11* (12), 2374−2381.

(13) Kawagoe, T.; Sato, S.; Jung, A.; Yamamoto, M.; Matsui, K.; Kato, H.; Uematsu, S.; Takeuchi, O.; Akira, S. Essential role of IRAK-4 protein and its kinase activity in Toll-like receptor-mediated immune responses but not in TCR signaling. *J. Exp Med.* **2007**, *204* (5), 1013−1024.

(14) De Nardo, D.; Balka, K. R.; Cardona Gloria, Y.; Rao, V. R.; Latz, E.; Masters, S. L. Interleukin-1 receptor-associated kinase 4 (IRAK4) plays a dual role in myddosome formation and Toll-like receptor signaling. *J. Biol. Chem.* **2018**, *293* (39), 15195−15207.

(15) Pereira, M.; Durso, D. F.; Bryant, C. E.; Kurt-Jones, E. A.; Silverman, N.; Golenbock, D. T.; Gazzinelli, R. T. The IRAK4 scaffold integrates TLR4-driven TRIF and MYD88 signaling pathways. *Cell Rep* **2022**, *40* (7), No. 111225.

(16) Fraczek, J.; Kim, T. W.; Xiao, H.; Yao, J.; Wen, Q.; Li, Y.; Casanova, J. L.; Pryjma, J.; Li, X. The kinase activity of IL-1 receptor-associated kinase 4 is required for interleukin-1 receptor/toll-like receptor-induced TAK1-dependent NFkappaB activation. *J. Biol. Chem.* **2008**, *283* (46), 31697−31705.

(17) Ackerman, L.; Acloque, G.; Bacchelli, S.; Schwartz, H.; Feinstein, B. J.; La Stella, P.; Alavi, A.; Gollerkeri, A.; Davis, J.; Campbell, V.; et al. IRAK4 degrader in hidradenitis suppurativa and atopic dermatitis: a phase 1 trial. *Nat. Med.* **2023**, *29*, 3127.

(18) Sun, D.; Zhang, J.; Dong, G.; He, S.; Sheng, C. Blocking Non-enzymatic Functions by PROTAC-Mediated Targeted Protein Degradation. *J. Med. Chem.* **2022**, *65* (21), 14276−14288.

(19) Burslem, G. M.; Crews, C. M. Proteolysis-Targeting Chimeras as Therapeutics and Tools for Biological Discovery. *Cell* **2020**, *181* (1), 102−114.

(20) Adhikari, B.; Bozilovic, J.; Diebold, M.; Schwarz, J. D.; Hofstetter, J.; Schroder, M.; Wanior, M.; Narain, A.; Vogt, M.; Dudvarski Stankovic, N.; et al. PROTAC-mediated degradation reveals a non-catalytic function of AURORA-A kinase. *Nat. Chem. Biol.* **2020**, *16* (11), 1179−1188.

(21) Gao, H.; Wu, Y.; Sun, Y.; Yang, Y.; Zhou, G.; Rao, Y. Design, Synthesis, and Evaluation of Highly Potent FAK-Targeting PROTACs. *ACS Med. Chem. Lett.* **2020**, *11* (10), 1855−1862.

(22) Tu, Y.; Sun, Y.; Qiao, S.; Luo, Y.; Liu, P.; Jiang, Z. X.; Hu, Y.; Wang, Z.; Huang, P.; Wen, S. Design, Synthesis, and Evaluation of VHL-Based EZH2 Degraders to Enhance Therapeutic Activity against Lymphoma. *J. Med. Chem.* **2021**, *64* (14), 10167−10184.

(23) Wu, Y.; Pu, C.; Fu, Y.; Dong, G.; Huang, M.; Sheng, C. NAMPT-targeting PROTAC promotes antitumor immunity via suppressing myeloid-derived suppressor cell expansion. *Acta Pharm. Sin B* **2022**, *12* (6), 2859−2868.

(24) Zhang, J.; Fu, L.; Shen, B.; Liu, Y.; Wang, W.; Cai, X.; Kong, L.; Yan, Y.; Meng, R.; Zhang, Z.; et al. Assessing IRAK4 Functions in ABC DLBCL by IRAK4 Kinase Inhibition and Protein Degradation. *Cell Chem. Biol.* **2020**, *27* (12), 1500−1509.

(25) Chen, Y.; Ning, Y.; Bai, G.; Tong, L.; Zhang, T.; Zhou, J.; Zhang, H.; Xie, H.; Ding, J.; Duan, W. Design, Synthesis, and Biological Evaluation of IRAK4-Targeting PROTACs. *ACS Med. Chem. Lett.* **2021**, *12* (1), 82−87.

(26) Nunes, J.; McGonagle, G. A.; Eden, J.; Kiritharan, G.; Touzet, M.; Lewell, X.; Emery, J.; Eidam, H.; Harling, J. D.; Anderson, N. A. Targeting IRAK4 for Degradation with PROTACs. *ACS Med. Chem. Lett.* **2019**, *10* (7), 1081−1085.

(27) Bekes, M.; Langley, D. R.; Crews, C. M. PROTAC targeted protein degraders: the past is prologue. *Nat. Rev. Drug Discov* **2022**, *21* (3), 181−200.
(28) Buckley, G. M.; Gowers, L.; Higueruelo, A. P.; Jenkins, K.; Mack, S. R.; Morgan, T.; Parry, D. M.; Pitt, W. R.; Rausch, O.; Richard, M. D.; et al. IRAK-4 inhibitors. Part 1: a series of amides. *Bioorg. Med. Chem. Lett.* **2008**, *18* (11), 3211−3214.
(29) Wang, L.; Ferrao, R.; Li, Q.; Hatcher, J. M.; Choi, H. G.; Buhrlage, S. J.; Gray, N. S.; Wu, H. Conformational flexibility and inhibitor binding to unphosphorylated interleukin-1 receptor-associated kinase 4 (IRAK4). *J. Biol. Chem.* **2019**, *294* (12), 4511−4519.
(30) Fischer, E. S.; Bohm, K.; Lydeard, J. R.; Yang, H.; Stadler, M. B.; Cavadini, S.; Nagel, J.; Serluca, F.; Acker, V.; Lingaraju, G. M.; et al. Structure of the DDB1-CRBN E3 ubiquitin ligase in complex with thalidomide. *Nature* **2014**, *512* (7512), 49−53.
(31) Li, P.; Jia, C.; Fan, Z.; Hu, X.; Zhang, W.; Liu, K.; Sun, S.; Guo, H.; Yang, N.; Zhu, M.; et al. Discovery of novel exceptionally potent and orally active c-MET PROTACs for the treatment of tumors with MET alterations. *Acta pharmaceutica Sinica. B* **2023**, *13* (6), 2715−2735.
(32) Ma, L.; Li, Y.; Luo, R.; Wang, Y.; Cao, J.; Fu, W.; Qian, B.; Zheng, L.; Tang, L.; Lv, X.; et al. Discovery of a Selective and Orally Bioavailable FGFR2 Degrader for Treating Gastric Cancer. *J. Med. Chem.* **2023**, *66* (11), 7438−7453.
(33) Qu, X.; Liu, H.; Song, X.; Sun, N.; Zhong, H.; Qiu, X.; Yang, X.; Jiang, B. Effective degradation of EGFR(L858R+T790M) mutant proteins by CRBN-based PROTACs through both proteosome and autophagy/lysosome degradation systems. *European journal of medicinal chemistry* **2021**, *218*, No. 113328.
(34) Wang, M.; Lu, J.; Wang, M.; Yang, C. Y.; Wang, S. Discovery of SHP2-D26 as a First, Potent, and Effective PROTAC Degrader of SHP2 Protein. *J. Med. Chem.* **2020**, *63* (14), 7510−7528.
(35) Kagan, J. C.; Su, T.; Horng, T.; Chow, A.; Akira, S.; Medzhitov, R. TRAM couples endocytosis of Toll-like receptor 4 to the induction of interferon-beta. *Nat. Immunol* **2008**, *9* (4), 361−368.
(36) Xiang, W.; Zhao, L.; Han, X.; Xu, T.; Kregel, S.; Wang, M.; Miao, B.; Qin, C.; Wang, M.; McEachern, D.; et al. Discovery of ARD-1676 as a Highly Potent and Orally Efficacious AR PROTAC Degrader with a Broad Activity against AR Mutants for the Treatment of AR + Human Prostate Cancer. *J. Med. Chem.* **2023**, *66* (18), 13280−13303.
(37) Schoenemeyer, A.; Barnes, B. J.; Mancl, M. E.; Latz, E.; Goutagny, N.; Pitha, P. M.; Fitzgerald, K. A.; Golenbock, D. T. The interferon regulatory factor, IRF5, is a central mediator of toll-like receptor 7 signaling. *J. Biol. Chem.* **2005**, *280* (17), 17005−17012.
(38) Pereira, M.; Durso, D. F.; Bryant, C. E.; Kurt-Jones, E. A.; Silverman, N.; Golenbock, D. T.; Gazzinelli, R. T. The IRAK4 scaffold integrates TLR4-driven TRIF and MYD88 signaling pat hways. *Cell Reports* **2022**, *40* (7), 111225.

https://doi.org/10.1021/acs.jmedchem.4c00181
J. Med. Chem. 2024, 67, 8060−8076